Realizing a Humanoid Neck With Serial Chain Four bar Mechanism

Yonas Tadesse, Kamesh Subbarao and Shashank Priya

Journal of Intelligent Material Systems and Structures published online 26 July 2010
DOI: 10.1177/1045389X10378775

Journal of Intelligent Material Systems and Structures OnlineFirst, published on July 26, 2010 as doi:10.1177/1045389X10378775

Realizing a Humanoid Neck with Serial Chain Four-bar Mechanism

YONAS TADESSE,[1,*,**], KAMESH SUBBARAO[2] AND SHASHANK PRIYA[1,**]

[1]*Automation & Robotics Research Institute, The University of Texas at Arlington, Fort Worth TX 76118, USA*

[2]*Department of Mechanical and Aerospace Engineering, The University of Texas at Arlington, Fort Worth TX 76118, USA*

ABSTRACT: In this article, we present design, fabrication, and characterization of a two-degree freedom humanoid neck based on serial chain four-bar mechanism. The nodding mechanism is designed in such a way that an eccentric center of gravity of the robotic head is counterbalanced by pre-tensioned springs which makes the modular neck prototype statically in equilibrium. In addition, due to installation of drive motor away from the rotation axis of nodding system, the torque requirement is significantly reduced allowing the use of low-cost RC servo motor to drive the head assembly. We describe in detail modeling and characterization of the neck rotational movement focusing on nodding mechanism. Extensive mathematical model for interaction of two dynamical systems, head–neck and servomechanism, is developed. Humanoid neck design based on RC servo motor having potentiometer feedback experiences inherent overshooting. In order to overcome the overshoot associated with servo dynamics, an external PD controller is implemented and the motion similar to that of human neck is demonstrated by numerical simulation.

Key Words: kinematics, actuators, four-bar mechanism, humanoid neck, degree of freedom, servo motor.

NOMENCLATURE

θ_a	Actuator rotation angle
θ_s	Actuator rotation angle with respect to horizontal axis
G_a	Amplifier gain
R_a	Amplifier output impedance
$\ddot{\theta}$	Angular acceleration
ψ	Angular acceleration coefficient
η	Angular position coefficient
$\dot{\theta}$	Angular velocity
ω	Angular velocity coefficient
T	Applied torque
E_m	Back electromotive force
Mr	Bearing friction torque
$\Delta\theta$	Change in head rotation angle
t	Clearance between the shaft and bearing
f	Coefficient of friction for roller bearing
C	Damping constant
T_d	Damping torque
d	Diameter of shaft supporting head
L	Distance of cg of head from pivot point
e	Error signal
G_g	Gear reduction
γ	Geometric constant
G	Generic function
g	Gravity
θ	Head rotation angle about point P from vertical
θ_f	Head rotation angle with respect to horizontal axis
x	Horizontal position of cg of head
I_x, I_y	Inertia of head
J_r	Inertia of the actuator
θ_p	Initial pre-tension angle of the spring from vertical axis
U_{in}	Input voltage
φ	Input voltage coefficient
λ	Kinematic variable
S	Laplace operator
L_1, L_2, L_3, L_6	Link lengths
M_h	Mass of head
J	Moment of inertia of the head assembly
K_m	Motor constant
I_m	Motor current
θ_o	Neutral position of the head from vertical axis
θ_f	Neutral position of the spring from horizontal axis
D	Outside diameter of bearing

*Author to whom correspondence should be addressed. E-mail: yonas@vt.edu
**Current address: Department of Mechanical Engineering, Virginia Tech., Blacksburg, VA 24061, USA
Figures 1–4 and 6–16 appear in color online: http://jim.sagepub.com

1045-389X/10/00 0001–23 $10.00/0 DOI: 10.1177/1045389X10378775

F_r Radial load
r Radius of servo horn
h Sensor gain
τ Shear stress
K Spring constant
F_s Spring force
θ' Spring rotation angle (large angle case)
y Vertical position of cg of head
μ Viscosity of oil
w Width of bearing

INTRODUCTION

THE design of humanoid face involves challenges at multiple levels and requires integration of technologies from various engineering disciplines. The hardware aspects of facial robotics involve physical appearance, actuation of key points on the face, tactile and distance sensing, speech, and vision system. The most notable humanoids are ASIMO (Sakagami et al., 2002), Albert-Hubo (Oh et al., 2006), and Repliee Q1 (Shimada et al., 2006). General descriptions and to some extent characterization of humanoid body parts has been discussed in literature (Albers et al., 2004; Berns and Braum, 2005; Hashimoto et al., 2006). This manuscript addresses the design and development of neck mechanism for a fully functional social robotic face which has the capability to interact with people visually, audibly, and physically. It demonstrates 16 kinds of facial expressions. A number of piezoelectric unimorph sensors were embedded inside the facial skin to respond to users' touch and thermal changes in the environment. This manuscript provides detailed mathematical model for the interaction of servomechanism and motor dynamics (driving force and torque) with the humanoid head. The problem is modeled as an interaction between two dynamical systems and the interconnection is determined via a detailed kinematic analysis. The full non-linear model is then simplified to enable near real-time implementation of action sequences. In what follows, the humanoid head and neck is discussed, followed by the realization of neck mechanism with a four-bar mechanism. Subsequently, the dynamical modeling is addressed and some representative simulations are presented that enable identification of the parameters in the dynamical model. This is followed by the results and discussion section and finally the conclusions are presented.

BACKGROUND

In this section, a brief review is presented on various neck structures and mechanisms reported in literature. Robonaut designed and developed by NASA Johnson Space Center has a neck mechanism, which is commanded by six-axis Polhemus sensor mounted on the teleoperators' helmet. The kinematics is based on a pan and tilt serial chain which provides it 2 DOF (Ambrose et al., 2000). Patane et al. (2004) presented the design of artificial vestibular system to sense head position and motion and then achieve coordinated neck-eye movement. An interesting neck mechanism, which utilizes multi-DOF ultrasonic servomotor, was proposed for tele-existence robot (Kawano et al., 2005). Such a motor has an advantage compared to the conventional servomotor in terms of noise control. However, the application of such motor is limited due to requirement of preloading mechanism and jaggy motion. A robotic head platform consisting of neck mechanism with 4 DOF kinematic chain has been constructed (Berns and Braum, 2005; Berns et al., 2006). All motions in this design utilized servo motor as an actuator. The fourth DOF was utilized for nodding motion which is separate from the rolling motion. The range of motion was $\pm 60^\circ$ about vertical, $\pm 30^\circ$ about horizontal, $\pm 30^\circ$ about frontal plane, and the fourth one was for nodding angle whose range was $\pm 40^\circ$. A 2-DOF neck with a serial mechanism has been proposed to mimic pitch and yaw of a head (Ouezdou et al., 2006). A 3-DOF parallel platform neck utilizing a spring, three tendons, and motors has been presented for yaw pitch and tilt (Jamone et al., 2006). The mechanism allows stiffness control but it requires pulling the motor all the time to keep the neck in a stiff position. This might lead to large consumption of power if the neck needs to be upright for most cases. Design analysis of two legs with Universal, Prismatic, Spherical Kinematic chain ($2UPS-1RU$) as a parallel platform for humanoid neck has been presented (Sabater et al., 2006). In this work, it was pointed that a spherical platform had difficulty to match with a work space required by a humanoid. The study provided tools to identify desired workspace of a humanoid neck and also constructed a workspace obtained from parallel platform.

Another type of neck utilized in humanoid robot SAYA (Hashimoto et al., 2006), includes a coil spring mounted on a disc, driven by Mckibben actuators for rolling & pitching and a DC motor for yawing. The tip of the head was subjected to flexion, extension, and lateral flexion with four tendons. The mechanism mimics the human cervical vertebra. However there is no further discussion to evaluate the performance of the system. Albers et al. (2003) have proposed a 3D model of neck joint that resembles a natural vertebral neck in terms of structure. The structure was composed of several discs connected by universal joints. The discs were driven by electric motors placed in torso via a rope that pulls each disc separately or all together. The ropes are guided by a neutral fiber within the neck. The mechanism mimics the architecture of a natural vertebral neck except that it requires several actuators to move individual cervical disc.

Kinematic modeling of head–neck movement have been conducted by Ouerfelli et al. (1999). The authors proposed tools to study kinematic parameters of the head

neck movement by using non-invasive identification method. It was found that two revolute (2R) linkages can model a sagittal plane movement. In fact, 3R or more revolute joints can also be used for modeling except certain constraints needs to be added in identification process. Sharkey et al. (1997) and Spiess and Vincze (1998), have discussed on the forward and inverse kinematics modeling aspect of robotic heads to assist researches in the area of active vision. Statistical measurement of neck motion from a subject group (two male and two female) has been conducted, which showed typical magnitudes of variables as 44° (standard deviation of $\sigma = 7.3°$) for rolling, 69° ($\sigma = 12°$) for yawing, and 110° for pitching with a maximum speed of 382°/s ($\sigma = 72°/s$) (Toshima et al., 2003).

Studying the biomechanics of biological neck enables us to understand the functionality of optimum system and possibly mimic its performance using artificial components. Basically, a human neck has several vertebra disc, ligaments, and muscles. The function of these muscles is to hold the head in erect position, to provide rotational motion, extension (head upward), and flexion (head forward) of the head. Two important muscles in the neck are known as trapezius and sternocleidomastoid muscles. These are located in the superficial connective tissue envelop of the neck. The trapezius is a broad flat muscle which covers most of the back side of neck. It is inserted into the occipital bone (located at the back and lower part of the cranium) and originates at the scapula in the thorax. The sternocleidomastoid muscle is a large thick bundle, which is easily seen in front of the neck. This muscle travels diagonally from its origin behind the ears to its insertion on the sternum (breastbone). The sternocleidomastoid muscles divide the neck into two regions, anterior and posterior regions. The posterior cervical compartment of biological neck includes cervical vertebrae and several deep muscles of the neck. Biological neck consists of seven cervical vertebrae. These vertebrae are connected with series of ligaments and joints (disc). Much of the extension and flexion movement of the head occur about the first cervical joint (C1), also known as atlas (Backaitis, 1993). In addition, due to the oval structure of the first cervical vertebra, only a forward and backward head rocking motion is allowed at this joint. The range of motion of this joint is approximated as the nodding gesture. The cervical vertebrae are stacked upon one another. The moveable joint has a fluid (synovial fluid) and it is through these joints that much of the neck movement is permitted (Huelke, 1979).

The seven cervical vertebrae of biological neck have different degree of freedom. The first one has 1 DOF and the remaining six have 3 DOFs each, but the angular motion of each is small. The overall range of motion is high because the neck is a long serial chain. In order to attain similar motion, a ball joint seems to be adequate but designing a drive mechanism for a ball joint is complicated. Rather, a simple kinematic joint 2R or 3R can provide satisfactory mechanism to mimic overall neck movement. Summary of DOF of various neck mechanisms proposed in the literature, type of actuators utilized, and other properties of various humanoids are provided in Table 1.

A linkage mechanism with actuator drive has wide varieties of application in robotics. A five-bar linkage with DC motors and MR brakes mechanism for 2 DOF haptic device (An and Kwon, 2009); a planar 3 DOF robotic arm with servomotor and shape memory actuators (Ashrafiuon et al., 2006); a six bar linkage mechanism with differential SMA actuator as a griper (Yan et al., 2007); a piezo composite actuator and four-bar mechanism for biomimetic fish design (Wiguna et al., 2009); a large number of actuators connected in series for discretely controllable manipulator (Lanteigne and Jnifene, 2008); and a 5R joint parallel platform for robotic manipulator (Rose et al., 2004) are some of the application linkage mechanisms reported in literature.

Smart materials have also been used for human robot interaction, either to dampen system dynamics or smoothen motion. In this regard, magnetorheological clutch has been developed for safe human robot collaboration (Saito and Ikeda, 2007). A damping system with magnetorheological fluid to overcome the velocity overshoot (Milecki and Sedziak, 2005) and pneumatic-based tendon drive system for lightweight robotic hand (Saga, 2007) have also been proposed.

HUMANOID HEAD AND NECK

The prototype robotic head used to develop the neck mechanism, utilizes the fabrication techniques described in detail previously (Hanson et al., 2006; Tadesse et al, 2006; Hanson Robotics Inc., 2009). Servo motors were utilized as actuators and installed inside a plastic skull. The brackets which hold the servos in position within the skull were designed for assembly and to withstand the reaction force of the servos. The motors were connected to the facial skin through anchor wires. These motors pull or push the skin through the anchors in order to generate the expression. The neck designed in this study has 2 DOF, nodding and turning. The nodding and turning of the neck is based on four-bar mechanism with 4R for nodding and RPRR (three revolute and one prismatic) for turning. A high torque servo motor controls the neck. Springs retain the balance between the center of gravity of the head assembly while the servos are not in action or in neutral state. Two CCD cameras, which serve as vision sensors, are installed in the eyes. The eyes and neck have the pan and tilt mechanism, which enables the robot to look left and right and move in the view direction. A CAD package is utilized to design all the structural components.

The system has 16 DOF with each eye and the neck joint having 2 DOF while the facial expressions have 10 DOF. The actuators are controlled by a Pololu

controller, which drives 16 servo motors by generating independent PWM (Pulse Width Modulation) signal and potentiometer feedback. The controller can receive the commands from the main computer and transmit the data to the main computer through RS232 interface. The specifications of the controller are shown in Table 2.

Figure 1 shows the picture of the solid model and the fabricated face with the embedded sensors and actuators of the robot head, Lilly. The skin material used for the physical appearance of robot is a commercially available platinum cured silicone material. Piezoelectric sensors are embedded in the skin at various locations such as ear, upper, and lower lips which enable the robot to respond to touch stimuli. The sensors are unimorph transducers consisting of a piezoelectric disc bonded to the brass disc. The diameter of the piezoelectric disc is 8 mm fabricated using the soft PZT material. The selection of piezoelectric unimorphs is based on the following

Table 1. Specification of full biped humanoid and humanoid heads with their neck mechanism.

Name	Total DOF	Neck DOF	Range	Neck motor	Actuator
ASIMO	24	2			Servo + Harmonic
(Sakagami et al., 2002)	3 DOF × 2 shoulder				
	1 DOF × 2 elbow				
	1 DOF × 2 wrist		N/A		
	1 DOF × 2 finger				
	3 DOF × 2 crotch				
	1 DOF × 2 knee				
	2 DOF × 2 leg				
ALBERT HUBO	66	3		3 servo motor	DC Servo motors +
(Oh et al., 2006)	31 DOF head facial emotion		N/A		
	35 DOF body motions				Harmonic reduction unit
REPLIEE	42	3			Air actuator
(Shimada et al., 2006)	13 DOF face		N/A		
	22 DOF arm				
	4 DOF lower back				
ROMAN	27	4	±60° vertical		DC Motors
(Berns and Hirth, 2006)	(just the head)		±30° horizontal		w/optical encodder
	3 DOF × 2 eye		±30° frontal		
	11 DOF face emotion		±40° nodding		
JAMES	22	3			Rotary motor
(Jamone et al., 2006)	4 DOF eye		N/A		(Faulhaber)
	7 DOF arm				
COG	21	3			DC electric motor with a series spring
(Brooks et al., 1998)	6 DOF arm × 2		N/A		
	3 DOF torso				
	3 DOF eyes				
BARTHOC	43°		N/A		
(Spexard et al., 2007)	10 DOF face				
WASEDA -4	29	4			
(Miwa et al., 2003)	21 DOF face		N/A		
	1 DOF lung				
	2 DOF waist				
DAV	43 Total	3			DC motor
(Han et al., 2002)	2 DOF torso				+
	7 DOF arm × 2		N/A		Anti-backlash gear motor
	8 DOF hand × 2				
	5 DOF head				
	3 DOF base				
KISMET	15 DOF face	3	N/A		Maxon DC servo motors
(Breazeal, 2004)	2 DOF ear				
YIREN	23 Total	2	40°/30° pitch		
(Tiejun et al., 2005)	7 DOF arm		−45°/45° Yaw		
	1 DOF hand				
	2 DOF waist				
ROBOTA	23	3	±80° yaw		Faulhaber
(Guenter et al., 2005)	3 DOF spine		±40° pitch		Motor
	7 DOF arm × 2		±30± roll		
	3 DOF eye				

N/A = not available.

criteria, (i) low profile, (ii) lightweight, (iii) fast response, and (iv) high capacitance. The small profile of the unimorphs allows them to be embedded inside the skin material without losing flexibility. The prototype robotic head, Lilly, has well-defined architecture for embedded sensors within the skin that facilitates human–robot interaction. Piezoelectric unimorph sensors around each facial feature can easily detect a touch stimuli and activate the verbal response from robot. This offers protection in cases where someone may apply damaging force to the robotic face. Details of the work related to sensing and human–robot interaction have been reported in Tadesse and Priya (2008).

DESIGN OF THE NECK MECHANISM

The turning and nodding function of the neck utilizes a four-bar mechanism, with 4R joints for nodding, and RPRR joints for the turning mechanism. The required angular motion is 60° (left and right) for turning (120° total) and 50° for total range of nodding angle. Schematic diagram of the neck mechanism is shown in Figure 2(a). The neck mechanism has 2 DOF and consists of two motors. A parallel linkage and spring helps stabilization of nodding and turning mechanism. Sleeve bearings are used at the joints in parallel linkage mechanism, and a thrust bearing is used at the center for the turning mechanism. As shown in Figure 2(b), the head inclines forward and backward when the servo motors 2 perform to and fro motion. The servo motor has a gear train, which is attached to each motor within the plastic housing to reduce the speed. The height of the motor is 31 mm and the total height of the neck mechanism is about 78 mm. Aluminum mounted self-lubricating sleeve bearing is chosen for the nodding mechanism because it is lightweight, corrosion-resistant, and can accommodate up to 5° of shaft misalignment and possesses SAE 20 viscous damping. Mounting bolts are incorporated in the mechanism; therefore, it is mountable on a biped robot. The serial chain mechanisms analyzed in this article provide desired kinematic trajectory. It is cost effective since each servomotor (model HS225MG) costs $30; simple to assemble and also reliable in terms of actuator life cycle due to the installation of motor away from the high torque pivoting point of the neck. A biological neck has seven cervical systems driven by several muscles. Emulating this platform with parallel mechanical system has advantage in terms of compactness, easy inverse kinematics, and high load-carrying capacity but still there are issues related to reduced workspace size. Therefore both nodding and turning were realized with serial mechanism.

The extreme kinematic positions of the nodding mechanism are illustrated in Figure 3. Dark lines indicate neutral position where the head is in upright situation, whereas, dotted and center lines represent maximum and minimum positions, respectively. The angles (θ_f and θ_s) measurements are taken with respect to the horizontal frame of reference.

Table 2. Specification of the controller.

Quantity	Value
PCB size	1.50″ × 2.275″
Servo ports	16
Resolution	1 μs (about 0.1°)
Range	250–2750 μs
Supply voltage	5.6–20 V
Data voltage	0 and 5 V
Pulse rate	50 Hz
Serial baud rate	1200–38,400 (automatically detected)

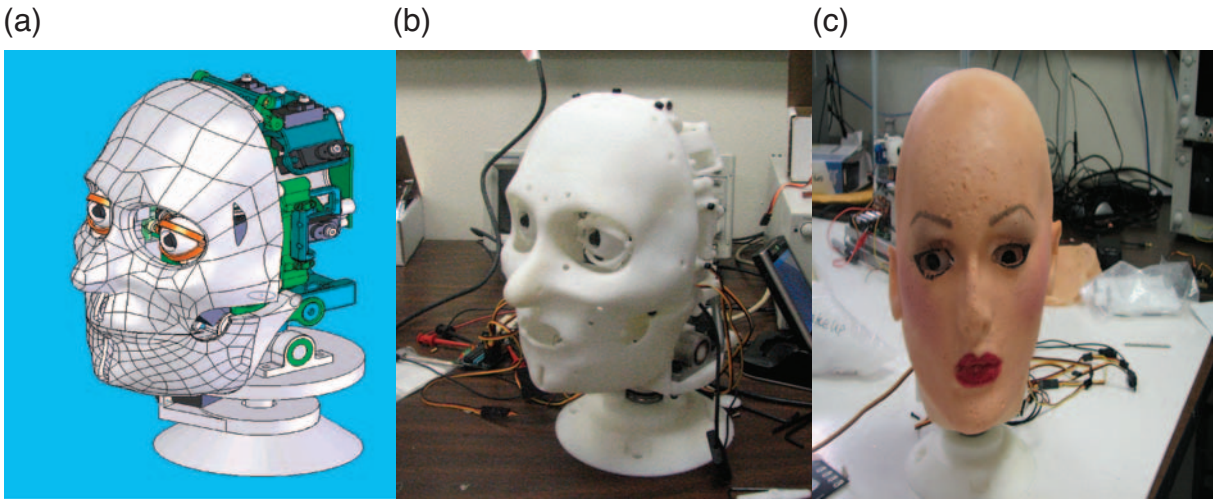

Figure 1. *Development of robotic head: (a) CAD model, (b) skull prototype, (c) fully functional face with embedded sensor within the skin of Lilly.*

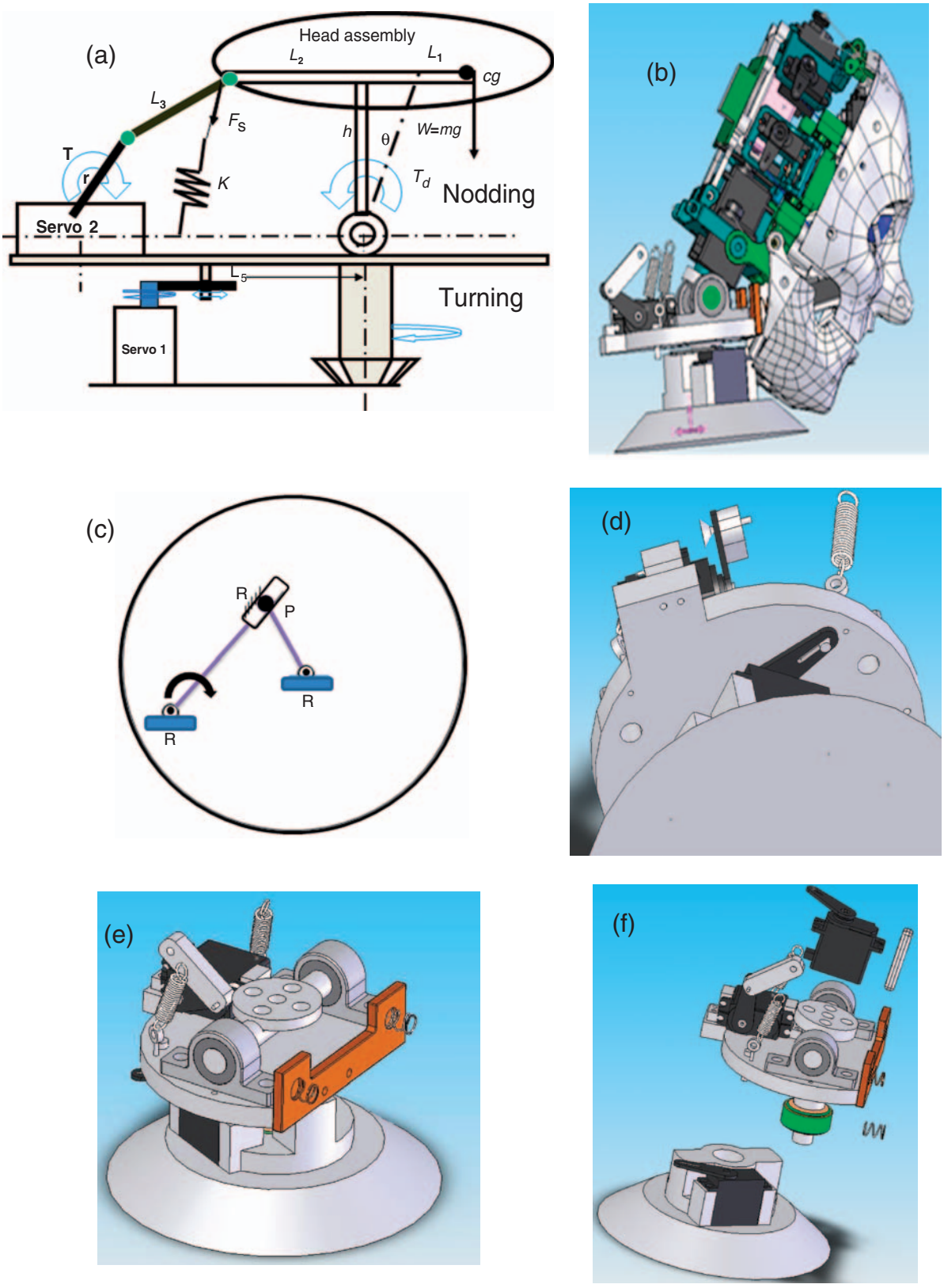

Figure 2. *Two degree of freedom humanoid neck: (a) schematic diagram of turning and nodding mechanism, (b) forward motion of the head, (c) schematic diagram of turning mechanism as observed from bottom, (d) oblique view of turning mechanism, (e) the modularity of the neck, (f) exploded view of the neck assembly indicating simplicity in assembly.*

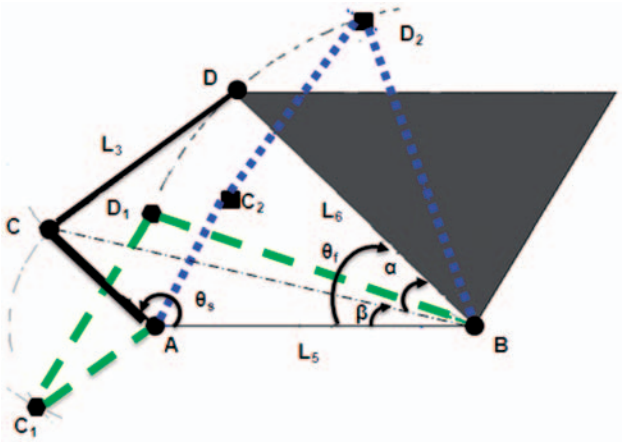

Figure 3. *Kinematic positions of the nodding mechanism.*

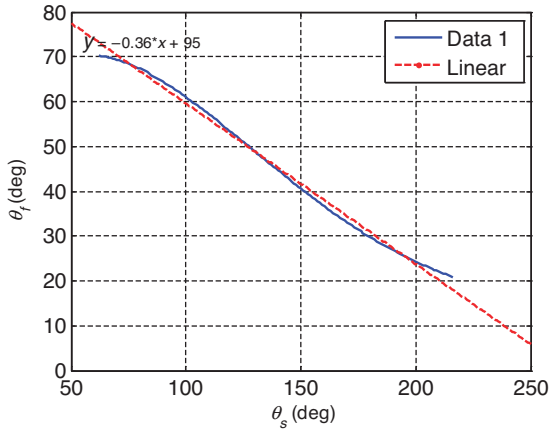

Figure 4. *Angular relationship between actuator and head angle with curve fit.*

Figure 3 shows three extreme kinematic positions of the nodding mechanism: (ACDB, neutral), (AC_1D_1B, upward), and (AC_2D_2B, downward). Applying sine and cosine law on triangle ABC provides:

$$BC = \sqrt{r^2 + L_5^2 - 2rL_5\cos\theta_s} = \lambda. \tag{1}$$

Again applying sine and cosine laws on triangle BCD, a functional relationship between actuator angle (θ_s) and head angle (θ_f) is given by Equation (2):

$$\theta_f = \beta + \alpha = \arcsin\left(\frac{r\sin\theta_s}{\lambda}\right) + \arccos\left(\frac{L_3^2 - \lambda^2 - L_6^2}{-2\lambda L_6}\right). \tag{2}$$

The parameters r, L_3, L_5, L_6 are link lengths, and are constants. The angle θ_f and θ_s are plotted with the best-curve fitting functions and demonstrated in Figure 4.

Figure 4 is a graphical representation of Equation (2), which is non-linear kinematic equation between the actuator angle θ_s and the head nodding angle θ_f, both measured with respect to the horizontal frame of reference. The data 1 in the plot was generated by setting θ_s to vary from 50° to 250° with an increment of 0.1° and by calculating θ_f according to Equation (2). The reason we plot this relationship is to distinguish the linearity range of two parameters and guide us to propagate the kinematic equation of the bar into the servo motor. For the range of angle considered (60°–220°), the linear function ($\theta_f = -0.36\theta_s + 95$) provides a reasonable estimate with a regression coefficient of 0.9945. Therefore, a change of the angular position of head $\Delta\theta_f$ and actuator angle $\Delta\theta_s$ can be written as:

$$\Delta\theta_s = \gamma\Delta\theta_f, \quad \theta_a = \gamma\Delta\theta. \tag{3}$$

The angles θ_a and $\Delta\theta$ are the positions with respect to the neutral position of actuator and the humanoid head, respectively. We note that Equation (2) provides a non-linear (transcendental) relationship between θ_f and θ_s. However, for the range of operation considered here, the relationship can be approximated by a linear one. Therefore, the attainable position of the head, the servo command, the change in actuator, and head angles can all be computed as shown in Table 3. Note that the target position signal ranges from 0–254 unsigned 8-bit integer while the servo motor is commanded with computer via RS232. When the neck nodding position is neutral (upright), the servo motor is set to be neutral by sending a zero 8-bit unsigned integer. Under this circumstance the actuator angle (column 4, θ_s in Figure 3) is set to be 135° with respect to the horizontal because it keeps the head upright. The other two rows, that is, upward and down position of neck are extreme values of the angles (θ_s, θ_f, θ_a, and $\Delta\theta$) when the head moves maximum upward and downward position. The target position column is the required 8-bit commands sent to the controller of the servomotor corresponding to each state. The column θ_a is the angular position of the actuator from its neutral position. It is obtained by subtracting the neutral position of θ_s from the max and min of θ_s row wise, that is, 81 = (216–135) and −73 = (62–135). Similarly the column $\Delta\theta$ represents the change in position of the nodding angle θ_f from the neutral position that is (25 = 45–20) and (−25 = 45–70).

For the turning mechanism, the high requirement of starting torque is overcome by using a low friction roller bearing. Roller bearings (anti-friction bearing) have a high loading capacity and exhibit very low rolling friction torques and hence low starting torque. The friction torques are similar or lower than ideally designed plain bearing operating under conditions of thick film lubrication. The coefficient of friction in roller bearings relates to the type of bearing, the speed of rotation,

Table 3. Neck positions and servo commands.

Neck position	Servo status	Target position Unsigned 8 bit	θ_s deg	θ_f deg	θ_a deg	$\Delta\theta$ deg
Upward	Maximum	127	216	20	81	25
Neutral	Neutral	0	135	45	0	0
down	Minimum	125	62	70	−73	−25

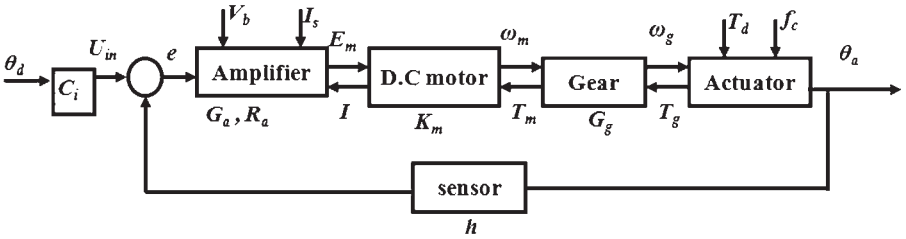

Figure 5. *Block diagram of servo motor and head.*

the load, and viscosity of lubrication. The bearing friction torque can be written as in Equation (4):

$$M_r = F_r \cdot f \cdot d/2 = F \cdot f_m \cdot D_m/2, \qquad (4)$$

where F_r is the radial (or axial) load, f is the coefficient of friction of rolling bearing, f_m is the coefficient of friction of rolling bearing based on mean diameter, d is the bore diameter of the bearing (shaft diameter), D is the outside diameter of the bearing, and $D_m = (d + D)/2$. Since the thrust ball bearing (axial load) has $f = 0.0013$, a reasonable estimate based upon the CAD model for coefficient of friction was determined to be 0.001 and the corresponding frictional moment was found to be 1.46×10^{-3} kg cm. As the starting torque is usually two-fold higher, within a reasonable load factor, the total torque was calculated to be 0.00876 kg cm. Further, as the center of gravity of the head is offset from the axis of rotation, two springs hold the face upright all the time while the servos are in neutral position. Therefore, the overall axial load of the robotic head will be applied on the center of thrust bearing. This in turn creates ease in tuning operation.

The schematic diagram of the nodding mechanism is illustrated in Figure 5. The mechanism uses all revolute joint (RRRR) with a spring to equalize the offset of the center of gravity. Therefore the neutral position of the head is maintained all the time. The nodding motion provided by the motor only needs an unbalanced force greater than zero. If springs are not utilized, then the servo motor has to provide a minimum torque that corresponds to the mass of the head (2.31 kg) and the offset distance (31 mm) from the pivoting axis, which should be greater than 9.9 kg cm. High torque servo motor such as HSR-5990TG ($125.00) or Dynamixel Dx-117 ($192) could have been used with increase in cost. However,

Table 4. Dynamic parameters of the head.

Properties	Units	Value
Density	kg/m^3	1000
Mass of skull	kg	0.97
Mass of skull with skin	kg	2.31
Volume	m^3	0.97×10^{-3}
Surface area	m^2	0.395
Center of mass		
X	m	0.140
Y	m	−0.077
Z	m	−0.024
Principal axes of inertia and principal moments of inertia taken at the center of mass		
Ix	kgm^2	2.240×10^{-3}
Iy	kgm^2	0.709×10^{-3}
Iz	kgm^2	0.075×10^{-3}

low cost servo motor such as HS225($30) with spring balance can do the desired task by maintaining the dynamic equilibrium. Both small angles as well as large angle approximation were considered in order to model the motion. The dynamic parameters of the head assembly shown in Table 4 are obtained from the CAD package, and these values are utilized for initialization of the dynamic system study of the head.

DYNAMIC MODELING

The dynamic model is similar to an inverted pendulum problem. The modeling utilizes a single lumped parameter model and the equations of motions are derived by considering equilibrium conditions in the *x*-, *y*-direction, geometric relationship, and moment about a point. The head can be simply considered as

an inverted pendulum and the values listed in Table 4 can be used for initialization of a Kalman filter or estimator, which is used as one of the tools for parameter identification. This avoids invoking the integral equations to find the moments of inertia of the skull, which has quite complex geometry. The servo assembly can be modeled as shown in the block diagram in Figure 5. The required actuator angle corresponding to desired head angle θ_d is provided to the system. This reference angle is converted into PWM, which can be further converted into an average voltage (U_{in}). The voltage is then applied on the closed-loop system. The output angle θ_a is derived from the basic equations of the components such as ideal DC motor, gear reduction ratio, and amplifier as shown in the block diagram in Figure 5 and derived as follows.

The error signal is obtained as a remainder from the input voltage and feedback angle as:

$$e = U_{in} - h\theta_a. \tag{5}$$

The back electromotive force (voltage) that drives the DC motor can be obtained by considering the amplifier block in the block diagram of the servo assembly and given as:

$$E_m = eG_a - R_a I_m. \tag{6}$$

The driving voltage and the angular speed are related by motor constant and can be expressed as:

$$E_m = K_m \omega_m. \tag{7}$$

Similarly, the torque of the motor and motor current are related by motor constant as:

$$T_m = K_m I_m. \tag{8}$$

The motor torque and output torque from the gear are related by a gear reduction ratio as:

$$T_m = G_g T_g. \tag{9}$$

Finally, from dynamic equilibrium of Newton's law for rotational system, the gear torque is equal to the sum of the rotational inertia and driving torque given as:

$$T_g = J_r \ddot{\theta}_a + T \quad \text{and} \quad \omega_m = \dot{\theta}_m. \tag{10}$$

Substituting Equations (5)–(9) into (10) and simplifying yields:

$$\frac{K_m G_a}{G_g R_a} U_{in} = J_r \ddot{\theta}_a + \frac{K_m^2}{G_g^2 R_a} \dot{\theta}_a + \frac{K_m h G_a}{G_g R_a} \theta_a + T. \tag{11}$$

Rearranging terms, changing into Laplace domain, and combining with Equation (3) and Equation (11) provides:

$$T = -J_r \gamma \Delta\ddot{\theta} - \frac{K_m^2}{G_g^2 R_a} \gamma \Delta\dot{\theta} - \frac{K_m h G_a}{G_g R_a} \gamma \Delta\theta + \frac{K_m G_a}{G_g R_a} U_{in}, \tag{12}$$

where K_m is the motor constant, G_a is the amplifier gain, R_a is the amplifier output impedance, G_g is the gear reduction, h is the sensor gain, J_r is the inertia of the actuator, U_{in} is the input voltage, S is Laplace operator, θ_a is the actuator rotation angle, and $\Delta\theta$ is head rotation angle. The angle θ_a and $\Delta\theta$ are related geometrically as shown in Equation (3).

The torque T can be derived from the dynamic equation of the head considering it to be an inverted pendulum. The free body diagram of the nodding mechanism is schematically depicted in Figure 6. Taking moment about a point P and applying D'Alembert's principle gives:

$$(M_h \ddot{y} - M_h g) L \sin\theta + M_h \ddot{x} L \cos\theta + J_{cg} \ddot{\theta} + T_d + F_s L_s - T = 0. \tag{13}$$

The geometrical relationship between x and y can be written as:

$$x = L \sin\theta \quad \text{and} \quad y = -L \cos\theta. \tag{14}$$

Therefore:

$$\ddot{x} = L\left(\ddot{\theta}\cos\theta - \dot{\theta}^2 \sin\theta\right) \quad \text{and} \quad \ddot{y} = L\left(\ddot{\theta}\sin\theta + \dot{\theta}^2 \cos\theta\right). \tag{15}$$

Substituting (15) into (13) yields:

$$\left(M_h L^2 + J_{cg}\right)\ddot{\theta} + T_d + F_s L_s - M_h g L \sin\theta - T = 0. \tag{16}$$

L_s is the moment arm of the spring at any general angle shown in Figure 6(a) and (b).

$$L_s = \frac{L_2 L_6 \sin\theta'}{\sqrt{\left(L_2^2 + L_6^2 - 2L_2 L_6 \cos\theta'\right)}} \quad \theta' = \theta_f \pm \Delta\theta \tag{17}$$

For small angle $\Delta\theta$ near the neutral angle, the arm length in Equation (17) will reduce to $L_s = L_2$, since $\sin\theta_f = (h_1/L_6)$. For small changes in angle, $\sin\Delta\theta \approx \Delta\theta$ and the restoring spring force can be written as:

$$F_s = K\Delta x = KL_6\Delta\theta. \tag{18a}$$

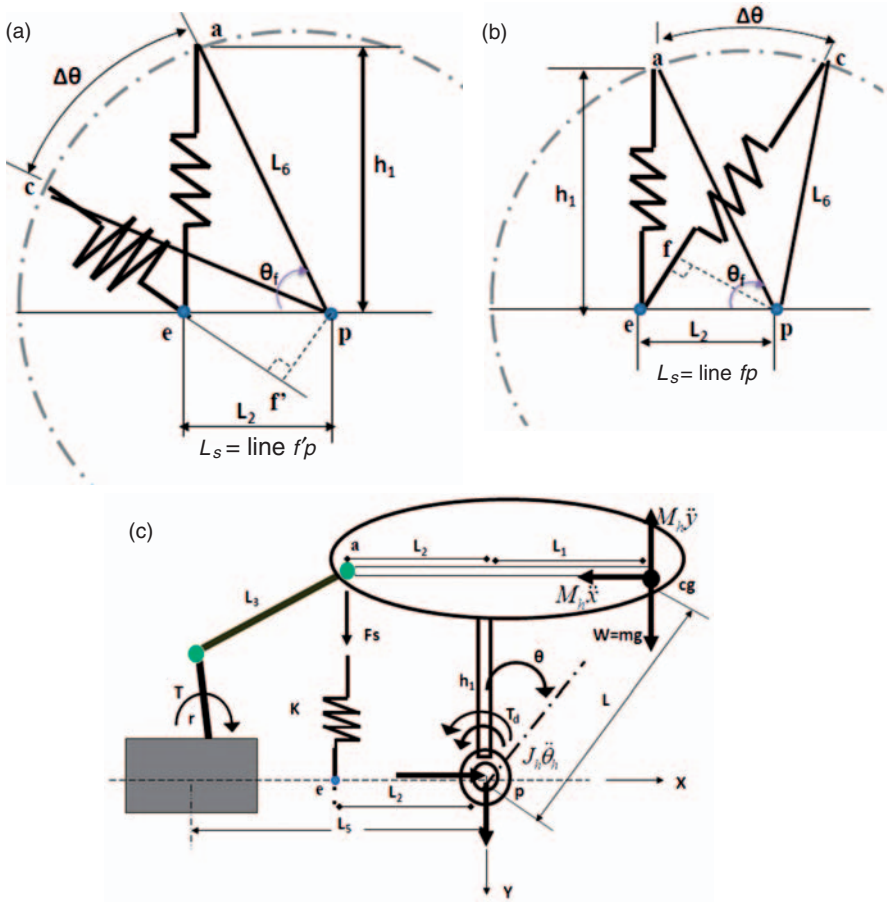

Figure 6. *Schematic diagrams representing: (a) spring position during upward nodding, (b) spring position during downward motion, and (c) free body diagram of the head nodding mechanism.*

However, when the head rotates the spring also rotates and changes its length at the same time. Under our aforementioned assumption of linear spring, the restoring force is then the product of the change in length at particular angle and the stiffness. Thus, the deflection is function of the angle of rotation. In reality, the spring bends somewhat along its midpoint. But the bending was ignored as its contribution to change in length is small. Hence for large angle the restoring force as shown in Figure 6(a) and (b) can be calculated as follows:

$$F_s = K\Delta x, \quad \Delta x = h_1 - \sqrt{\left(L_2^2 + L_6^2 - 2L_6L_2\cos\theta'\right)}, \tag{18b}$$

The lubrication within the shaft brings about damping in the system. According to fluid mechanics, for low Reynolds number, the damping at bearings can be approximated by the following equations for shear stress on the surface of a rotor shaft:

$$\tau = \mu\frac{\mathrm{d}U}{dt}\left(\approx \mu\frac{\Delta U}{\Delta t}\right). \tag{19}$$

$\mathrm{d}t$ represents the thickness of fluid film and $\mathrm{d}U$ is the velocity of the fluid in the shaft.

The velocity profile at the surface is given as:

$$U = \Delta\dot{\theta}\cdot d/2, \tag{20}$$

$$T_d = (\tau A)\cdot d/2, \quad A = 2\pi\,\mathrm{d}w. \tag{21}$$

Combining Equations (19)–(21) yields:

$$T_d = \mu\left(\frac{\mathrm{d}U}{\mathrm{d}t}\right)(\pi d^2 w) = \left(\frac{\pi\mu d^3 w}{2t}\right)\Delta\dot{\theta} = C\Delta\dot{\theta}. \tag{22}$$

Inertia of the links is usually small as compared to the head; therefore it is neglected in the modeling equation. Replacing the damping term and considering the static equilibrium condition ($\ddot{\theta} = \dot{\theta} = 0$) without torque applied by the motor, Equation (16) can be written in a linear form as:

$$F(\theta) = F_sL_s - M_hgL\sin\theta = 0. \tag{23}$$

At neutral angle, θ_0, assuming the spring is elongated from initial pre-tension angle, θ_p:

$$F(\theta_0) = K\left(\theta_0 - \theta_p\right)L_6L_2 - M_hgL\sin\theta_0 = 0. \tag{24}$$

Therefore, Equation (16) can be linearized by defining small angle, $\Delta\theta = \theta - \theta_0$, replacing θ with $\Delta\theta + \theta_0$ and using low order Taylor series expansion about equilibrium position θ_0 as:

$$\begin{aligned} F(\theta_0 + \Delta\theta) &= F(\theta_0) + F'(\theta_0)\Delta\theta \\ &= (KL_6L_2 - M_hgL\cos\theta_0)\Delta\theta. \end{aligned} \tag{25}$$

Hence Equation (16) becomes:

$$\left(J_{cg} + M_hL^2\right)\Delta\ddot{\theta} + C\Delta\dot{\theta} + (kL_2L_6 - M_hgL\cos\theta_0)\Delta\theta = T, \tag{26}$$

$$I_z = \int \left(y^2 + x^2\right) \mathrm{d}m, \quad \text{and} \quad J = J_{cg} + M_hL^2, \tag{27}$$

where J is the moment of inertia of the head assembly, θ is the rotation angle of head about point P, K is the spring constant, L_1, L_2, L_3, L_6 are link lengths, M_h is mass of head, T is torque, d is diameter of shaft supporting head, W is width of bearing, and t is thickness of the clearance between the shaft and bearing. Combining Equations (12), (22), and (26) gives the relationship between output angle and input voltage as:

$$\frac{\Delta\theta}{U_{in}} = \frac{\left(K_mG_a/G_gR_a\right)}{\left(\begin{array}{l}(J + \gamma J_r)S^2 + \left(C + K_m^2\gamma/G_g^2R_a\right)S \\ \quad + \left(K_mhG_a\gamma/G_gR_a + KL_2L_6 - M_hgL\cos\theta_0\right)\end{array}\right)}. \tag{28}$$

The input voltage (U_{in}), which is proportional to desired position of actuator, is provided from driving software as:

$$U_{in} = C_i\theta_d. \tag{29}$$

Equation (28) provides information about the parameters that affect the performance of angular movement under the simplification and assumptions, in order to study the dynamic behavior of nodding angle. The above system can be represented in a simplified second-order form as:

$$\frac{\Delta\theta}{U_{in}} = \frac{c}{S^2 + aS + b}. \tag{30}$$

Again, for large angles, combining Equations (12), (16), (17), and (18b) gives us a parametric Equation (31):

$$\begin{aligned} &\left(M_hL^2 + J_{cg} + J_r\gamma\right)\ddot{\theta} + \left(C + \frac{K_m^2}{G_g^2R_a}\gamma\right)\dot{\theta} + K\Delta xL_s \\ &\quad - M_hgL\sin\theta + \frac{K_mhG_a}{G_gR_a}\gamma\theta - \frac{K_mG_a}{G_gR_a}U_{in} = 0. \end{aligned} \tag{31}$$

The left side of equation can be written as one generic function of all parameters:

$$G\left(\ddot{\theta}, \dot{\theta}, \theta, U_{in}, M_h, g, \ldots,\right) = 0 \tag{32a}$$

Taylor series expansion about an equilibrium angle θ_0 of Equation (32) is given as:

$$\begin{aligned} G - G_0 = &\left.\frac{\partial G}{\partial\ddot{\theta}}\right|_{\theta_0}\left(\ddot{\theta} - \ddot{\theta}_0\right) + \left.\frac{\partial G}{\partial\dot{\theta}}\right|_{\theta_0}\left(\dot{\theta} - \dot{\theta}_0\right) + \left.\frac{\partial G}{\partial\theta}\right|_{\theta_0}(\theta - \theta_0) \\ &+ \left.\frac{\partial G}{\partial U_{in}}\right|_{U_{in0}}(U_{in} - U_{in0}) = 0, \end{aligned} \tag{32b}$$

where G is the generic function and G_0 is the functional value of G evaluated at equilibrium point (angle). Using the partial derivative evaluated at the equilibrium point, changing the variables in terms of change in the parameter, and substituting in Equation (32b) yields:

$$\psi\Delta\ddot{\theta} + \varpi\Delta\dot{\theta} + \eta\Delta\theta + \varphi\Delta U_{in} = 0, \tag{33}$$

where $\psi = M_hL^2 + J_{cg} + J_r\gamma$

$$\varpi = C + \frac{K_m^2}{G_g^2R_a}\gamma$$

$$\eta = K\left(\frac{\partial\Delta x}{\partial\theta}L_s + \frac{\partial L_s}{\partial\theta}\Delta x\right)\Bigg|_{\theta_o} - M_hgL\cos\theta_o - \frac{K_mhG_a}{G_gR_a}\gamma$$

$$\frac{\partial\Delta x}{\partial\theta} = -\frac{0.5c_2\sin\theta_f}{\sqrt{\left(c_1 - c_2\cos\theta_f\right)}}$$

$$\frac{\partial L_s}{\partial\theta} = \frac{\left(\left[c_2\cos\theta_f\right]\left[\left(c_1 - c_2\cos\theta_f\right)\right] - 0.5\left[c_2\sin\theta_f\right]^2\right)}{2\left[\left(c_1 - c_2\cos\theta_f\right)\right]^{3/2}}$$

$$c_1 = L_2^2 + L_6^2 \quad c_2 = 2L_6L_2 \quad \Delta\theta = \theta' - \theta_f = \theta - \theta_o$$

$$\varphi = -\frac{K_mG_a}{G_gR_a}$$

Remarks:

1. We note that the form of dynamics in Equation (33) can easily be cast in the form of Equation (30).
2. For the purpose of implementation of the servo control loops for real-time operation, we simply use an appropriate initial set of values for the neck angle and let the control loops compensate for the errors.

Dynamic Model Parameter Estimation

The angle measurements were done using a combined LabVIEW and MATLAB program. The LabVIEW program was used to drive the servo motor and the MATLAB program was used to extract the angle

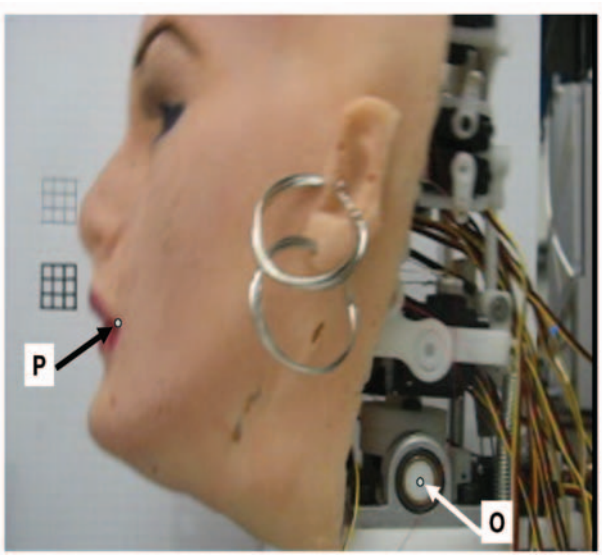

Figure 7. *Angle measurement from video frames.*

measurements. The experimental procedure was as follows. First, a target position of the actuator angle was provided from the LabVIEW program. The signal was sent through a serial port to the controller and the motion of the head was recorded by a camera. Next, an audio-video (AVI) file was stored in a directory and from each frame, the pixel coordinates of the tip of the mouth (P) and centroid of the shaft (O) were exported to a workspace. The positions were then stored and the angles were measured by simply taking the tangent of the vertical line to the horizontal line. The frame rate of the camera was 15 which meant that the time interval of measurement was 1/15 (0.067 s). Figure 7 demonstrates the measurement steps.

Image processing has been used widely to determine quantitative data from video footage. There are several instances where image processing has been successfully demonstrated in extracting a useful data Huang (2000). This technique is especially useful for complicated system where position transducers are difficult to mount due to space constraint or if the system has been designed without the embedded transducer. To exemplify, image processing has been used for pyramid angle determination of a helicopter rotor with CMOS camera (Mai et al., 2009) and for medical imaging and computer integrated surgery (Yao and Taylor, 2003) depending on the optical components used for video capturing. In addition, image processing has been shown to provide high precision angle measurement with accuracy of 0.01 arc sec (1.67 e-4 deg) (Yuan and Long, 2003). It is also known that image processing will incur error due to image noise, image distortion, and optical aberration.

The choice of angle measurement from video frame in this study is primarily due to the non-invasive nature of extracting the angle information from video sequence. The frame rate of camera was 15 (the measurement interval is 0.067 s). Secondary potentiometer or encoder could have been used on the joints to measure the angle but the available space was quite small. It should be noted that servo motors do have their own potentiometer to measure the current angle of the rotor shaft but the output was connected to the circuitry on servo driver chip and was unavailable. The angle of interest for the humanoid neck nodding was the one pivoting about point O as shown in Figure 7.

The accuracy of angle measurement at each frame is dependent on the contrast between the tip of the mouth and background. The lipstick used on the mouth creates a good contrast between the cheek and the mouth. Figure 8(a) shows lines drawn from the pivoting axis to the tip of the mouth in one of the frames of the video file. A red solid line being true position was constructed by a point obtained with a default threshold value using edge detection of the mouth. Let us say the edge is not accurately estimated and falls within 6 pixel radius and maximum 10 pixels radius. Two erroneous lines, blue dashed and green hyphenated lines drawn with points on the circles, are shown in Figure 8(b). If the edge falls in the vicinity of 6 pixel radius, the angular error from the pivoting axis P will be 0.28°. Whereas, if it is 10 pixel the maximum error will be 0.68°. Cropped image, traced boundary, binary filled image, and the filled image with two circles bounding uncertain points from the edge of the mouth are shown in Figure 8(c)–(f) to illustrate angular measurement and error that are associated with image processing in MATLAB.

The parameters a, b, and c in Equation (30) were determined from the angle measurements. The output angle of the head was measured for a step input voltage. An extended Kalman filter (EKF) was applied to determine the constants by initializing the parameters considering the equivalence of Equations (28) and (30). The dynamic parameters taken were the damping term C, moment of inertia J, and the KL_2L_6 terms. Since the moment of inertia of the actuators was much less than the head assembly, it was ignored. The damping term C was calculated from Equation (22) using viscosity of $\mu = 125\,\text{Ns/m}^2$ for SAE 20 lubrication and was equal to $0.0532\,\text{Nms}$ ($d = 12.7 \times 10^{-3}\,\text{m}$, $w = 15.8 \times 10^{-3}\,\text{m}$, $t = 0.12 \times 10^{-3}\,\text{m}$). Note that the lubrication was provided in the two shaft support. The damping term T_d torque is a velocity-dependent coefficient of friction due to the lubricant and it affects the dynamic system. Damping is usually an uncertain term and changes in long period of time due to wear, tear, and lubricant condition. If the velocity $\dot{\Delta}\theta$ is assumed to be constant and the operating speed to be half of the no load speed (no load speed of HS $225 = 0.11\,\text{s}/60°$), the damping torque will be 0.252 Nm. This is higher a value as compared to the stall torque of the motor (HS 225 stall

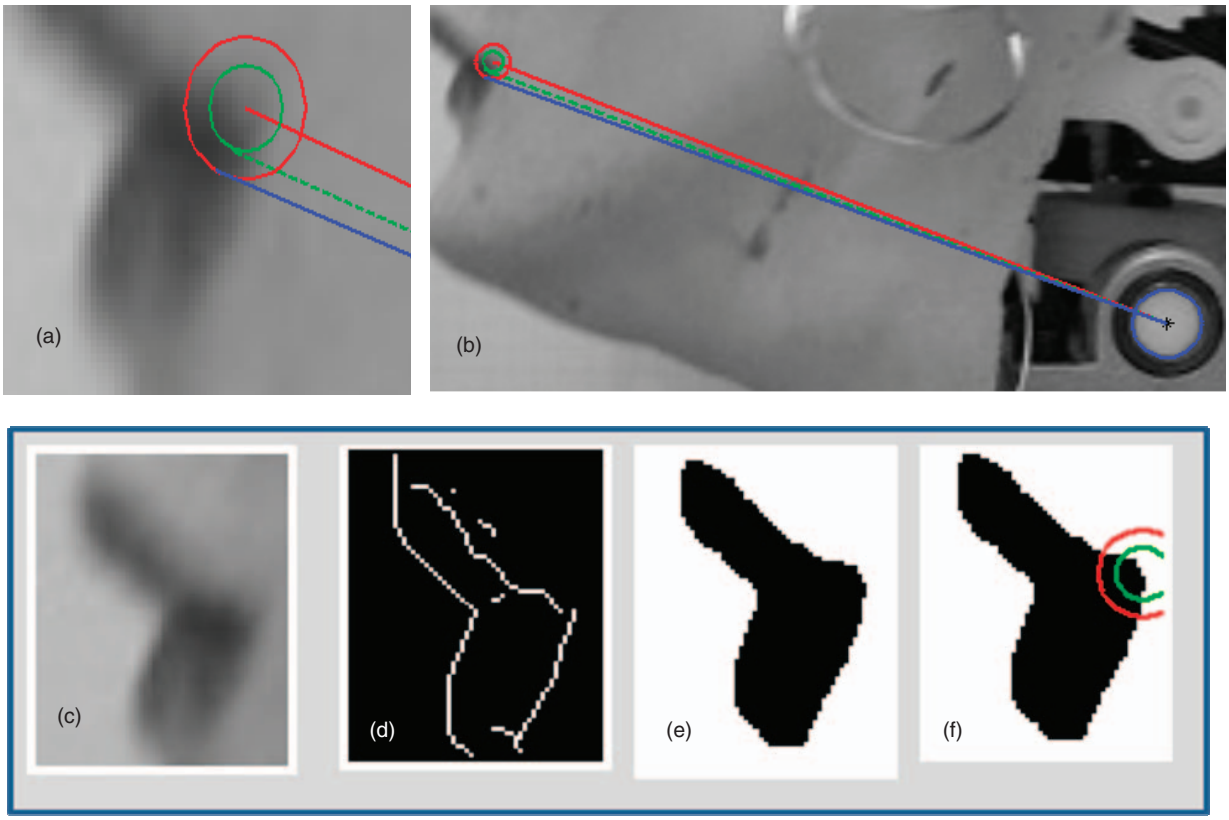

Figure 8. *Angle measurement accuracy: (a) zoomed mouth, (b) lines from pivoting axis, (c) cropped image, (d) edge detection with Canny filter, (e) binary boundary filled, (f) filled boundary with circles enclosing uncertain edge points.*

torque = 4.8 kg cm = 0.47 Nm. Therefore it cannot be ignored. The other constants used in the calculation were: spring stiffness = 10.72 lb/in (1877.8 N/m), $L_2 = 48 \times 10^{-3}$ m, $L_6 = 59 \times 10^{-3}$ m, mass of the head $m = 2.319$ kg and moment of inertia from Equation (20), $J = 0.0058$ kgm^2 ($J_{cg} = 0.075 \times 10^{-3}$ kgm^2, $M_h = 2.31$ kg, $L = 50 \times 10^{-3}$ m). For simple estimation, only the inertia J, damping coefficient C, and known constant term KL_2L_6 terms were considered with two decimal points ($J = 0.01$, $C = 0.05$, and $KL_2L_6 = 5.31$). Substituting the above parameters in Equation (28) and normalizing, the initial values for parameter estimation in Kalman filtering were determined to be as: $a = 5$, $b = 531$, and $c = 100$. The initial value of the gain c was further adjusted by first plotting the step response of 22° angle and observing a factor that shifts the graph to fit the measured angle and was found to be 529. A MATLAB program was utilized to find the constant using EKF algorithm. Changing the initial condition in the vicinity of the parameters described above ($a = 5$, $b = 531$, and $c = 520$), the model constants in Equation (30) converge to the values of $a = 25.9786$, $b = 523.7292$, and $c = 507.5597$ (the default MATLAB program provides four significant digits). The main motive of raising EKF on this portion is to illustrate that the dynamic parameters obtained from the CAD model as shown in Table 4 can be used to initialize Kalman filter. It was just an explanation to extend the knowledge of system identification from the parameters available at hand. Let us name system identified in this section as SYS1.

Kalman filtering was used to find the constants of the second-order equation. It was initialized by using Equation (28) and the known terms namely, inertia of the head (J), viscous damping coefficient (C), and the term (KL_2L_6), to simplify the estimation as described in Equation (30). This will help to use the available values as initial values for the estimation instead of guessing initial values with arbitrary constant. In the EKF program, the measurement error covariance (r) was 0.0001 and initial covariance chosen was $P_o = 1000*I$ [5 × 5]. The process noise covariance (Q) value was 0.001. Several trials were made with different values of r and this value seems to be good for both first measurement and confirmation. The process noise covariance was also changed but this did not change the simulation result by significant degree. The initial values were varied and simulation was conducted; however, best results were not observed in both first and second test with series of step inputs. The constant values presented here represent the best fit for all the measurement sets. The program was also tested with synthetic data with known

Gaussian noise (standard deviation $\sigma = 0.5$) generated by a second-order transfer function with known terms $a = 4$, $b = 45$, and $c = 1000$. The known terms were determined by EKF and the estimates converged to $a_m = 3.7$, $b_m = 42.3$, and $c_m = 938$ (the subscript 'm' is used to differentiate actual and estimated values). The initial values during estimation were $a_0 = 3$, $b_0 = 40$, and $c_0 = 900$ with $r = 0.5$. This shows that the program used for estimation is free from error.

The vectors of the estimated parameter of the nodding system dynamics change from the initial estimate to the final values. The 'a_m' value changes from 5 to 26 and the 'b_m' and 'c_m' values did not change significantly from the initial estimate. The large change in the coefficient of 'a_m' suggests that the originally assumed value of damping term was not accurate enough.

In fact, the overall Equation (30) could be second- or third-order model depending on whether the inductive load is considered or not. But to simplify the neck mechanism design, let us consider the second-order system given in Equation (30). Once parameters were identified, one can relate those constants (a, b, c) with the coefficients in Equation (28). Since there are many parameters, it is difficult to find explicit relationship between the parameters identified (i.e., a, b, c) and the remaining parameters (K_m, G_a, G_g, h, etc.). However, the constant parameters of the servo motor (K_m, G_a, G_g, h, etc.) can be taken to find the rest of the parameters.

Based upon the above analysis, the neck designing can be summarized as follows:

1. Choose a mechanism. As explained in the literature review, a 3R or higher order system can provide desired trajectory and in this article 4R mechanism was realized.
2. Take measurement sets for nodding, turning angle of an individual to be emulated by the robotic head. For a 3 DOF neck, a rolling motion can be included and the measurement could be done in various non-invasive ways.
3. Obtain a functional relationship for the mechanism realized in the first step and determine the parameters with system identification. For example: for second-order system presented here, parameters a, b, and c.
4. Determine other parameters (K_m, G_a, R_a, h, etc.) from prior experimentation or from data sheet of manufactures catalog or through separate characterization for the motor. (Steps 3 and 4 are interchangeable).
5. Relate the identified parameters with various constants to get desired performance. For instance: from the ratio of 'a' to 'c' we can determine the damping constant C if the rest are fixed. Let us define the constants $c_3 = (K_m G_a / G_g R_a)$, $c_4 = (K_m / G_a G_g)$ and $c_5 = G a^2 / R_a$ The product, KL_2L_6 can be obtained from 'b' to 'c' ratio. A combination of parameters can be chosen by fixing one and varying the other.

$$\frac{a}{c} = \frac{C + K_m^2 \gamma / G_g^2 R_a}{K_m G_a / G_g R_a} . = \frac{C + c_3 c_4 \gamma}{c_3} \tag{34a}$$

$$\frac{b}{c} = h\gamma + \frac{KL_2L_6 - M_h g L \cos\theta_n}{K_m G_a / G_g R_a} = h\gamma + \frac{KL_2L_6 - M_h g \cos\theta_n}{c_3} \tag{34b}$$

6. Therefore the neck mechanism design can choose parameter r, L_3, L_5, L_2, L_6, and K according to the relations obtained and also constraints imposed by the dynamic model and geometrical relationship. For example, for a given M_h, g, L, and θ_n, once b and c are obtained from system identification, if K_m, G_a, G_g, R_a are obtained from other resource, the choice of link parameter and spring stiffness needs to satisfy Equation (34b) and the stability criteria of Equation (35). The necessary condition for stability of the dynamic system is that the characteristic polynomial term should be greater than zero:

$$K_m h G_a \gamma / G_g R_a + KL_2L_6 - M_h g L \cos\theta_n > 0 \tag{35}$$

The inertias of the links length do not affect the dynamic significantly and it was ignored. The parameter r, L_3, L_5 do not appear in the dynamic Equation (28) directly. Their effect is included with the geometric parameter γ. The link parameters however determine the overall range of motion. Therefore, they can be chosen to satisfy range of motion.

7. The natural neck movement is similar to a damped system response. Once the modeling parameters are determined in open loop, a feedback control will take care of the desired performance (such as rise time, settling time, etc.). But the main objective of demonstrating the modeling equation is that the system characteristics can be influenced by the choice of material before control action takes place. This is particularly useful to optimize a given design in terms of dimension, mass, and cost.

This completes the design of neck to satisfy certain geometric (range of angles) and dynamic criteria (rising time and settling time). The above description is a guideline to choose the parameter based on several simplification and assumptions in order to model the system as a simple second-order system. To illustrate the outline described in this section, let us consider the analysis on neck prototype. For the current problem $a = 26$, $b = 524$, and $c = 508$ it was assumed that the moment of inertia of the head was valid ($J = 0.0058\,\text{kgm}^2$), the inertia of the actuator J_r was

ignored (it was of the order of 10^{-10} kgm^2), then from the equivalence of Equations (28) and (30), the term $(K_m G_a)/(G_g R_a) = c\ J = 2.95 = c_3$. In the current design, we know the value of K, L_2, L_6, M_h, L, and θ_o. From 'b' to 'c' ratio, we can get the value of feedback gain $h = 1.39$. The stability criterion Equation (35) suggests that $h < 4.26$. The 'a' to 'c' ratio, provides the value of $c_4 = -0.09$. However, the constant c_4 cannot be negative because the K_m, G_a, and G_g are all positive. Therefore the a/c ratio suggests that the initial damping constant term is underestimated. This could be due to inaccuracy of taking parameters in Equation (23) such as clearance between the shaft and the bearing (t). Hence, the a/c ratio can only provide the relationship between C and $C4$. On the other hand, let us say the motor parameters are known ($K_m = 3.3 \times 10^{-3}$, $G_a = 37$, $G_g = 1/12$, $R_a = 0.5$), the feedback gain $h = 1.39$ and the identified constants are same as before ($a = 26$, $b = 524$, and $c = 508$). Design is often an iterative process so the geometrical parameter (r, L_3, L_6, L_5) should be chosen first to determine γ. For $r = 25$ mm, $L_3 = 41$ mm, $L_5 = 55$ mm, $L_6 = 59$ mm, γ can be determined from the slope of actuator angle and head angle, as in Figure 4 ($\gamma = -0.36$) and then, $c_3 = (c)(J) = (508 \times 0.0058) = 2.95$, $c_4 = (K_m/G_a G_g) = 1.07 \times 10^{-3}$, from a/c ratio, the damping term C can be obtained ($C = 0.15$) and b/c ratio gives the product of the terms KL_2L_6 to be 5.32. If any of these parameters change, the response of the neck will also change. Effect of each parameter is dealt in the following section by numerical simulation.

For the overshoot observed in the servomechanism, a controller could dampen the neck nodding response. However, realizing neck parameters beforehand helps to reduce the controlling aspect. It is assumed that various individuals do have different responses. Some people can turn their head fast and some not (various rise time), some move at large angle and some not (range of motion). Normally the overshoot of an individual neck angle is minimum or purely damped. Therefore, realizing the neck from such perspective helps in devising a methodology to improve the performance. For instance, improving the viscous damping C or the motor constant ameliorates the overshoot. Also introducing derivative controller improves the overshoot performance. The effect of the external spring K utilized to balance the head and the link length L_6 along with the mass of the head influences the response in terms of rise time and overshoot.

NUMERICAL SIMULATION

To study the effect of variables on the overall angular movement of the nodding response and explain how the modeling equation described in the previous section can be used, numerical simulations were carried out utilizing the second-order Equation (28). To this end, practical values of the variables described in Equation (28) (i.e., h, K_m, G_a, etc.) were utilized as listed in Table 5. These are average values that will be varied in the upper and lower bound from mean values. The torque constant of the motor (K_m) of miniature DC electric motor of similar size (Johnson permanent DC flat motor, 15–20 mm diameter) was 3.3 mNm/A (DC Micromotors, 2010). The gear reduction ratio (G_g) was found by counting the gear teeth and taking their ratio after disassembling the servo motor. The PCB of the Hitec HS225MG servo has a driver IC (hitech rcd HT7003) and the detail of the IC and its characteristics were not provided by the vendor. Effort was made to find information of the IC from manufacturer but was not successful. Therefore, the values of amplifier gain and output impedance were estimated based on other known values in literature. General amplifier gain (G_a), can attain a range from 5–1000 depending on the resistance (Analog Devices, 2010). The output impedance was usually low. Typical operational amplifiers can have output impedance less than 1 Ω. The feedback gain of some potentiometer ranges from 1–6 V/rad (Goyal and Bakshi, 2007; Kulakowski et al., 2007). The moment of inertia of the rotor shaft was obtained from $l_x \frac{md^2}{8}$ where m is the mass of the rotor and d is the diameter of the rotor shaft. The other values of parameters listed are discussed in the previous section.

Table 5. Variables of simulation.

Parameter	Value	SI Unit
Torque constant	$K_m = 3.3$ e-3	Nm/A
Amplifier gain	$G_a = 37$	–
Gear reduction ratio	$G_g = 1/12$	–
Amplifier output impedance	$R_a = 0.5$	Ω
Moment of inertia of head assembly	$J = 0.0058$	kgm^2
Rotor inertia	$J_r = 0.11475$ e−10 (steel shaft, diameter = 1 mm and length = 15 mm)	kgm^2
Geometric factor	$\gamma = -0.36$	–
Damping in the shaft	$C = 0.15$	Nms
Feedback gain of potentiometer	$h = 1.4$	V/rad
Stiffness of the spring	$K = 1877.8$	N/m
Link length L_2	$L_2 = 48$ e−3	m
Link length L_6	$L_6 = 59$ e−3	m
Mass of the head	$m = 2.319$	kg
Neutral angle of head	$\theta_o = 45$	deg
Gravity	$g = 9.81$	m/s^2
Length from pivoting position to center of gravity	$L = 50$ e−3	M

The numerical simulation result using the values listed in Table 5 and Equation (28) are shown in Figure 9 for step input response. The value of one variable was changed keeping the other constants to study how the variables affect the response of the system. In most cases, the rise time is about 0. s. As can be seen in Figure 9(a) and

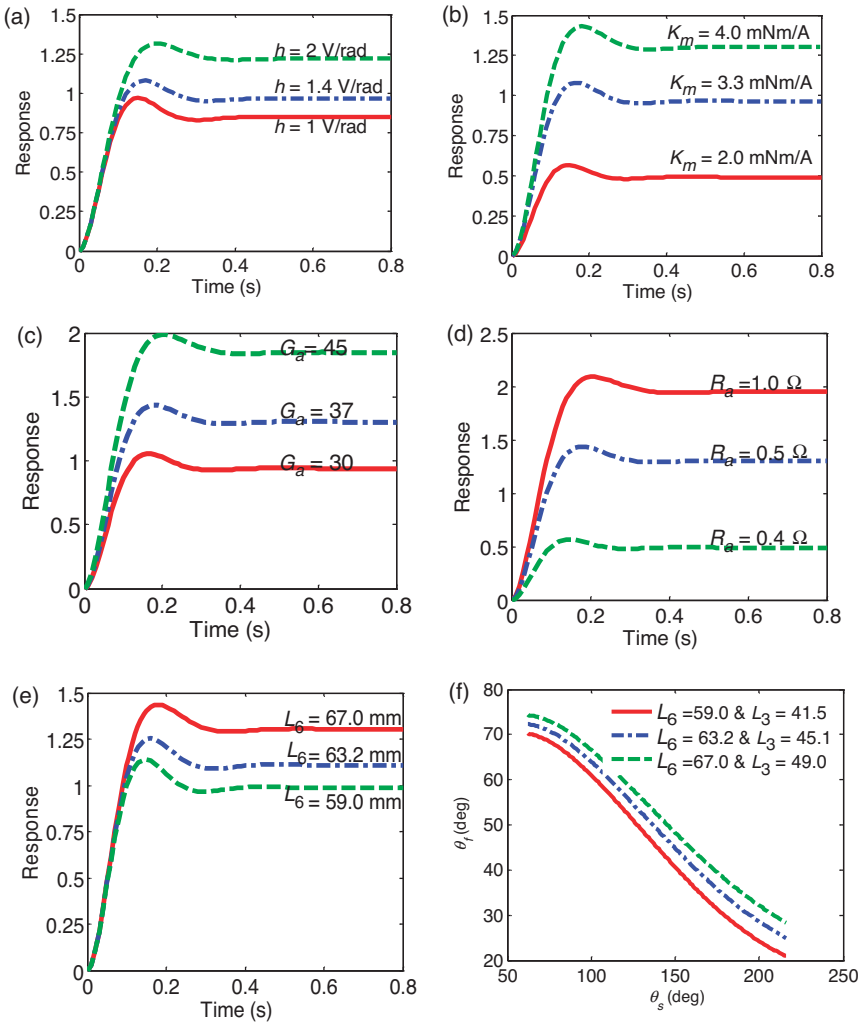

Figure 9. *Numerical simulation result: (a) feedback gain, h effect; (b) motor torque constant, K_m effect; (c) amplifier gain, G_a effect; (d) output impedance, R_a effect; (e) link length, L_6 and geometric parameter γ effect; (f) geometric parameter relationship between θ_f and θ_s.*

(b), a 0.4 V/rad change in feedback gain exhibits a small change in overall amplitude of response whereas a 0.7 mN/A change in torque constant K_m, has a large effect on response. In Figure 9(c), a five order of magnitude difference in the amplifier gain, G_a, brings about significant change in the response as seen in Figure 9(d), a 0.5 Ω change in the output impedance, R_a changes the response amplitude significantly. Figure 9(e) illustrates the effect of the change in link length L_6 and the associated geometric parameter γ to keep the closed form of the four-bar mechanism. Since as L_6 changes, L_3 also changes and therefore the geometric parameter γ is changed accordingly. Figure 9(f) shows how the geometric parameter γ changes as the L_3 and L_6 change.

RESULTS AND DISCUSSION

A second-order mathematical relationship was created between the estimated angle and input voltage corresponding to desired angle. The parameters were obtained from the estimation in the previous section (SYS1). The estimated and measured angles are plotted and shown in Figure 10(a). It can be inferred from this figure that the head reaches its commanded steady-state angle of 22° within 1.2 s. The overshoot from the measured angle is 14% and the rise time is 0.4 s while the model in the previous section (SYS1) estimated 10% overshoots. Therefore, the model prediction based on physically available data needs more rigorous system identification. We will discuss a more accurate prediction model and design adaptation in the next sections. Several table top tests indicate that the head assembly is stable for both turning and nodding actions. Further improvements can be done by using position sensors on the head shaft and applying different controller such as PD to reduce overshoot.

The nodding angle of an adult male subject was measured in order to compare the response of neck mechanism with that of designed neck. The measured angle is plotted in Figure 10(b). It can be inferred from this

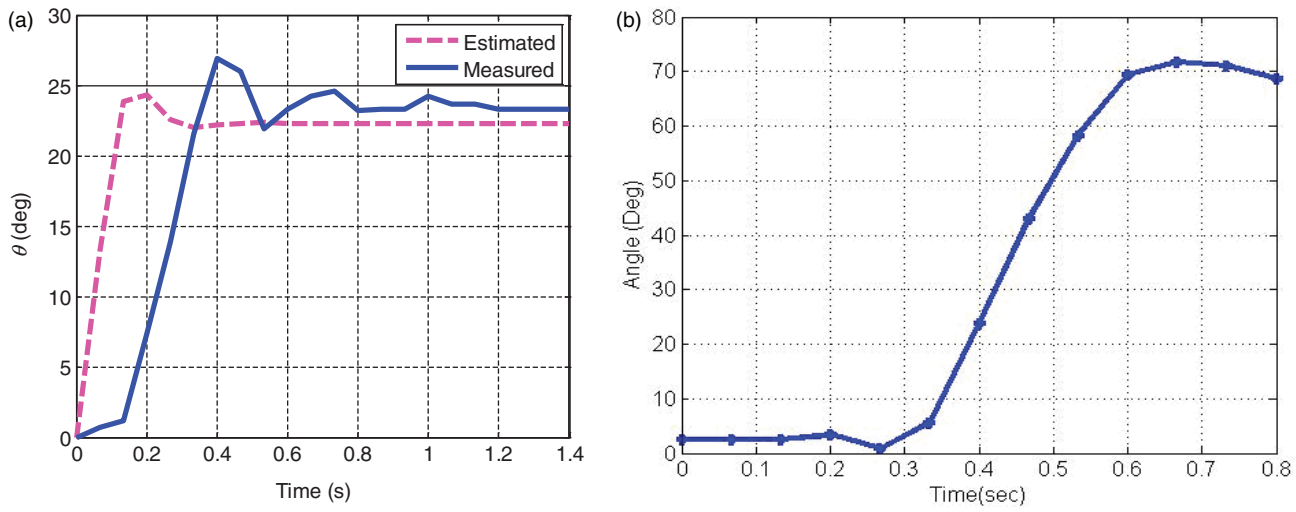

Figure 10. *(a) Experimental and estimated value of nodding angle using SYS1, (b) Nodding angle of an adult male.*

figure that it takes 0.3 s to reach the maximum angular position of 70°. Therefore, the rise time is about 0.3 s with minimum overshoots or (damped system response). The motion was smooth and reaches steady state quickly. The biomechanical response of human movement such as nodding exhibits a reflex action similar to that of damped mechanical system. The muscles of the neck around the cervical areas are all voluntary type, which are directed by the will of the individual. The extensional voluntary movement of the neck as in Figure 10(b) is initiated by increasing neural activation, which then triggers the extensional movement of the muscles at the anterior side followed by a braking movement applied by the muscle at posterior side. The damped system response is mainly due to the sequential muscle activation. The intrinsic damping properties of muscles, ligaments, tendons, and fluidic nature are insufficient to provide the damped system characteristics. Comparing Figure 10(a) and (b), the rise time was found to be 0.4 s for the neck prototype presented in this study and 0.3 s for the biological neck. This result shows a good matching between the time responses considering the simplifications made in the design of neck. Further, Figure 10(a) shows that experimental measurement has a decaying overshoot with settling time slightly longer than that of biological neck. It is known in the literature that human muscle consists of 80% fluidic substance (Heymsfield et al., 1983; Wang et al., 1999; Bedogni et al., 2002; Rudenko and Sarvazyan, 2006). But the fluidic nature of the muscle alone is not sufficient to demonstrate a damped system characteristics. The model presented here was also verified by applying a series of step input and the results indicate that the estimate closely follows experimentally measured nodding angle. Figure 11 illustrates the various input signals, the measurement, and estimated angle.

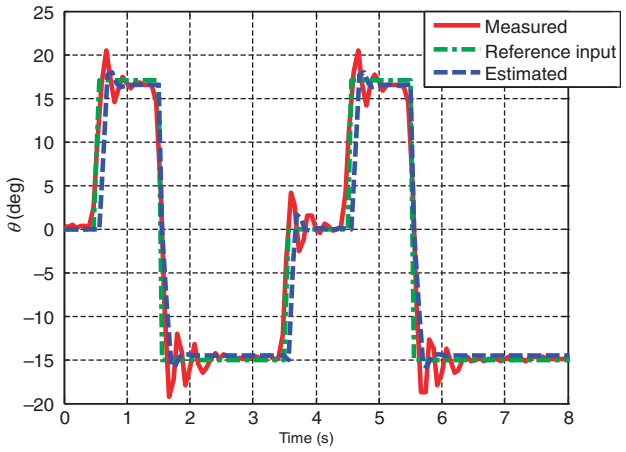

Figure 11. *Verification of the model with various step input and initial condition using SYS1.*

The servo motors consume significant magnitude of power. At no load condition, one servo motor requires about 6 V when driven with a step input and in the continuous drive condition the voltage goes down to 3.5 V with current consumption reaching 0.6 A. The total power consumption of single servo motor is 2.1 W. Figure 12(a) and (b) shows the voltage requirements for several cycles of nodding and turning. Figure 12(a) is the voltage consumption directly measured by using NI data acquisition cards. The driving servo motor for the nodding motion consumes 6 V at the beginning and drops down to 3 V at higher current amplitudes during actuation. The voltage consumption during the turning motion drops from 6 to 3.5 V as shown in Figure 12(b). The difference between these two results is related to the ease of movement and load imposed on the servo motor. It was found that nodding motion requires higher power than turning which is related to the fact that as the

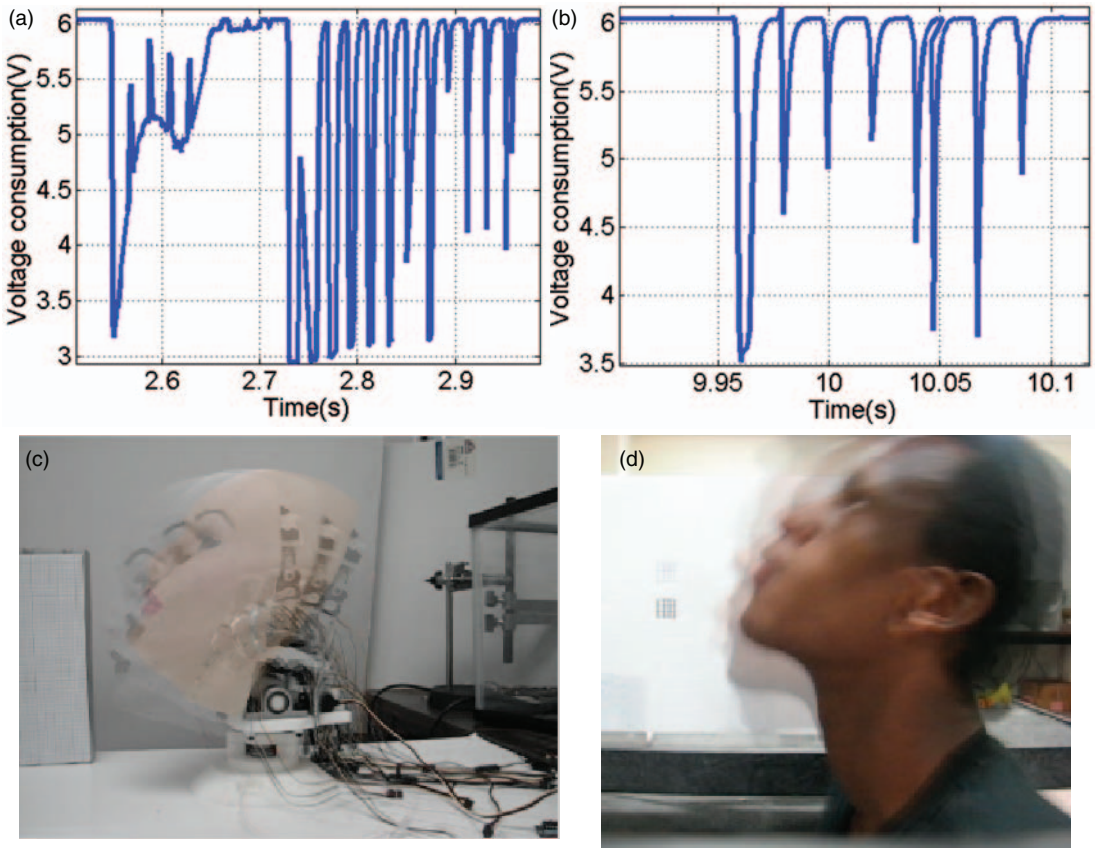

Figure 12. *Servo motor voltage consumption during (a) nodding (b) turning mechanism and comparison of nodding step of (c) the robotic head (d) an adult male subject.*

center of gravity of head changes it applies extra load on the servomotor. During the turning motion, the center of gravity remains vertical for the entire duration. The robotic head has a total of 16 servo motors, (2 DOF neck/14 DOF facial movements) where one servo motor consumes about 2.1 W. If all of the servo motors are simultaneously driven which is not the case practically, then the total power consumption for fully functional face will be 33.6 W ($2.1 \times 16 = 33.6$ W). This explains the problem in utilizing servo technology; however, in the absence of any competitive alternative they remain the prime choice.

The voltage drop in Figure 12 seems to be unnatural or due to limited power supply. Topward 3306D DC power supply capable of providing 30 V and current up to 6 A was utilized with all knobs set at maximum. On close observation it can be seen that on the time axis the voltage drop occurs within 100 ms for nodding and 50 ms for turning. This shows that the voltage was not changing abruptly and taking certain time to rise up and down. It should be noted here that the actuation was done by changing the control signal (slider bar with unsigned integer) in a LabVIEW program manually.

Experimentally determined step motion of the nodding angle of robotic head and typical human nodding angle are presented for comparison in Figure 12. The video stream of the motion in both cases was captured using a MATLAB program. The corresponding angles between each frame were also extracted. The images at each discrete step are displayed by varying alpha parameter using the Image Processing Toolbox. The alpha parameter is a variable that controls the Laplacian filter of an image acquisition in MATLAB. It makes the image blurred, sharp, or original depending on its value which ranges from 0.0 up to 1.0. The step motion of the nodding angle of the robotic head and adult male subject are shown in Figure 12(c) and (d).

The above voltage consumption is for a random movement of the neck but if we set the position to move in regular periodic command position the voltage consumption will also be uniform. Figure 13. shows the uniformity of the voltage across the servo terminal.

Remarks:

1. We note that the simplified dynamical model for the neck mechanism as in Equation (30) was able to predict the actual motion quite closely.

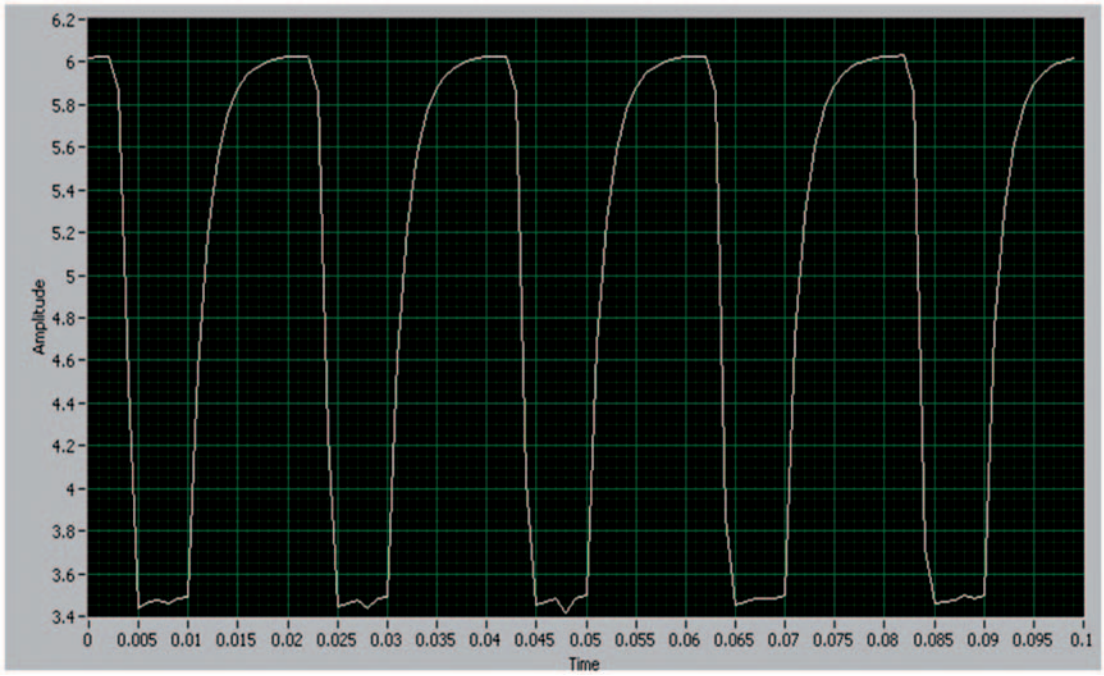

Figure 13. *Voltage consumption of turning motion for a step change of 127–137 servo position (0–255 unsigned integer values correspond to a 0°–180° servo arm rotation).*

2. The rise time (10–90%) values and settling times were almost similar but the steady-state values were off by about 4°. We also note an initial delay in the actual response that was not captured by the linear model.
3. It should be emphasized that the main focus of this work was to evaluate the effectiveness of the linear modeling and we can see that gross trends were captured sufficiently well.
4. As mentioned earlier, the parameter values in Equation (30) were dependent on the initial neck angle and since they were evaluated just once, the behavior of the actual dynamics is little different from the linearized prediction. That said, this simple linear model was sufficient for real-time servo-loop implementation. The steady-state errors were easily handled by introducing an integrator in the compensator.

A more detailed system model using the MATLAB System Identification Toolbox was derived to be as follows: A third-order prediction error estimate of a general linear model was obtained based on the step response of the neck mechanism. The system identification was performed based on an output error method:

$$\frac{\theta(s)}{U(s)} = \frac{47.3859\left(s^2 + 56.8s + 980.1\right)}{(s + 13.22)(s^2 + 12.29s + 149)}. \qquad (36)$$

We note that the predicted model does not have the exact structure of the linear model in Equation (30). This is attributed to the fact that several simplifying assumptions were made in deriving the model in Equation (30). Let us call the system identification given by Equation (36) as SYS2. The time-domain responses for the actual and the predicted cases are plotted in Figure 14.

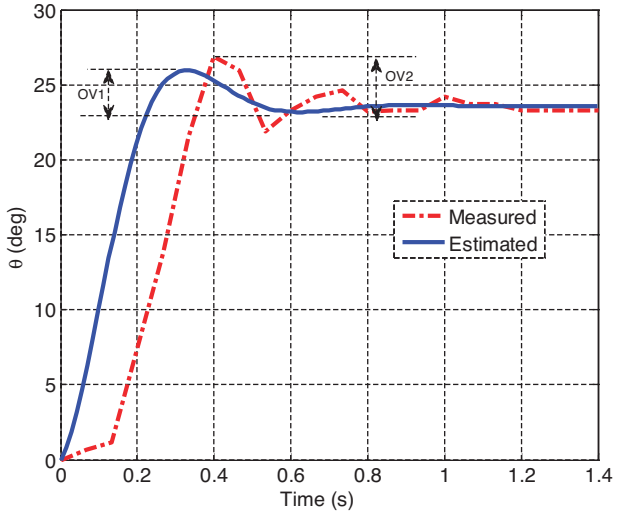

Figure 14. *Step response comparisons between estimated angle with SYS2 and measured nodding angle of the robotic head (overshoot values OV1 = 10% and OV2 = 14%).*

Notice that the predicted response still does not capture the initial delay but the rise time, overshoot, settling time, and the steady-state values are very nicely captured

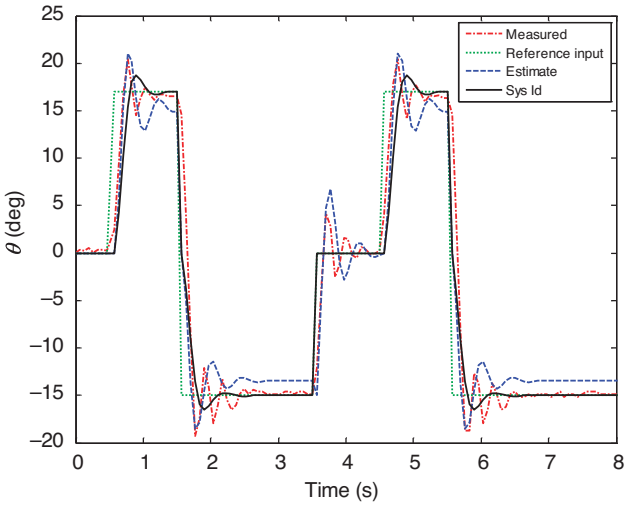

Figure 15. *Verification of the model (SYS2) with various step and initial condition input.*

by this new model. Further experiments are underway to refine this model. The overshoot was 10% (OV1) and clearly indicates that the model predicts the experimental value of overshoot 14% (OV2). Finally, the verification of the system identification model with various step and initial condition input in comparison with the second-order estimate and the measured values is shown in Figure 15.

It can be seen from Figure 15 that the model identified via the system identification approach (SYS2) was very efficient in capturing the actual model responses. It is imminent that the system has potential overshooting in all series of step test. This overshoot associated with servo dynamic can be overcome by using an external PD controller. To this end, if a PD controller with gain of K_p and K_d are introduced in a negative position feedback along with the plant transfer function described by Equation (36), the closed loop transfer function can be obtained as given in Equation (37).

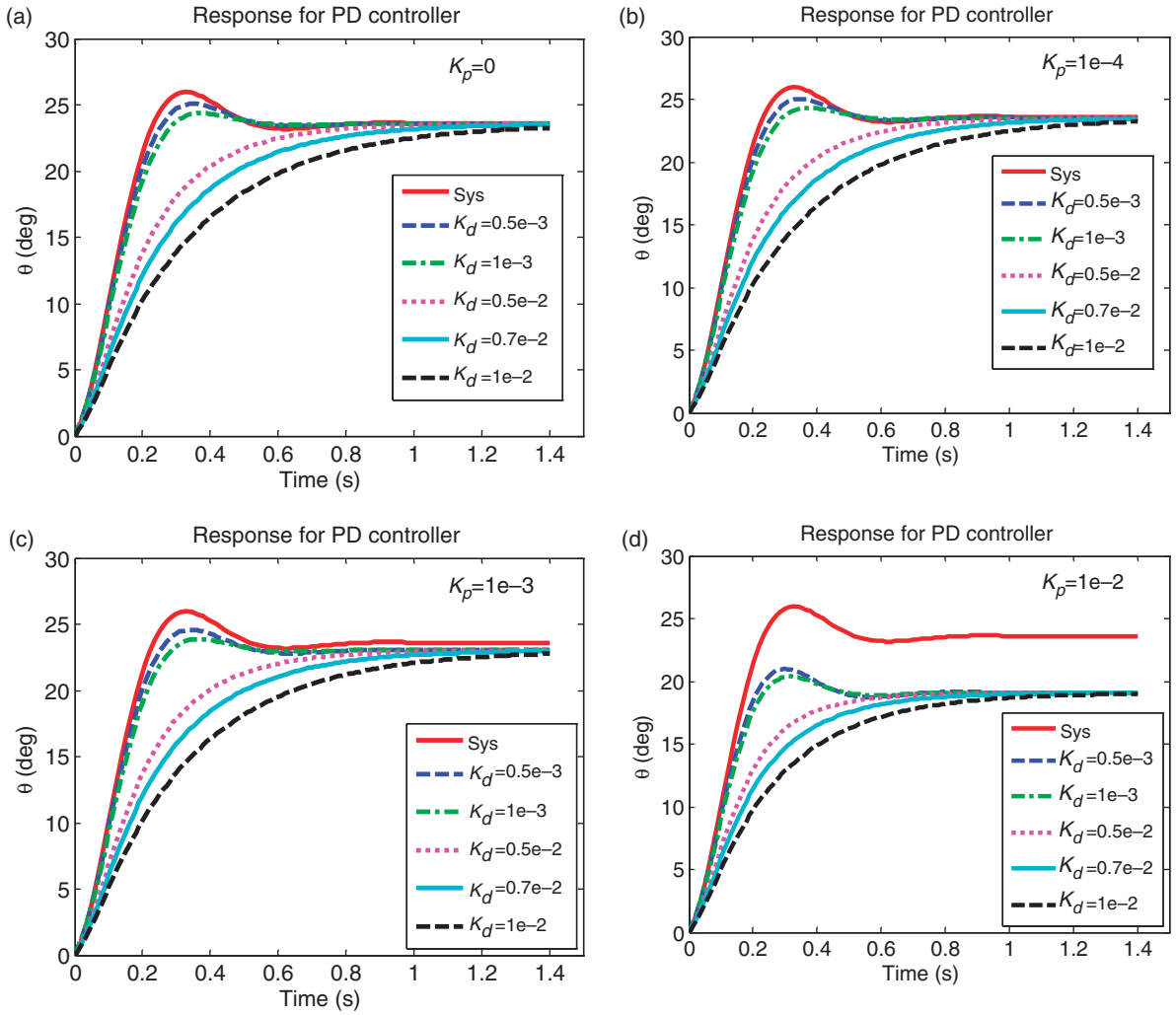

Figure 16. *Response for PD controller of neck nodding motion simulation with various proportional (K_p) and dervative (K_d) gain constants using Equation (37).*

The overshoot can be minimized and the response can be damped similar to biological neck as illustrated in Figure 10(b). The parameters of the gain were varied and simulations were carried out to find the values using Equation (37). A derivative constant K_d between 0.5×10^{-2} and 10^{-2} reduces the overshoot as shown in Figure 16(a)–(d) while a proportional constant $K_p = 0$–10^{-4}, provides minimum steady-state error as demonstrated in Figure 16(a)–(d). However, large constant $K_p = 10^{-2}$ introduces large steady-state error. Therefore a feedback gain $K_p = 0$–10^{-4} and $K_d = 0.5 \times 10^{-2}$ to 10^{-2} leads to a good combination of gain constants, which provides a damped system response like the biological neck. Damped response of human neck subject has been reported by Toshima et al. (2003), Mertz and Patrick (1993), Lee and Terzopoulos (2006), Zafar et al. (2002), and Pedrocchi and Ferrigno (2004).

$$\frac{\theta(s)}{U(s)} = \frac{g_1\left(s^2 + a_2 s + a_3\right)}{\left(\begin{array}{l}(1 + g_1 K_d)s^3 + \left(b_2 + g_1\left(K_p + a_2 K_d\right)\right)s^2 \\ \quad + \left(b_3 + g_1\left(a_2 K_p + a_3 K_d\right)\right)s + \left(b_4 + g_1 a_3 K_p\right)\end{array}\right)}, \tag{37}$$

where $g_1 = 47.385$, $a_2 = 56.8$, $a_3 = 980.1$, $b_2 = 25.5$, $b_3 = 311.5$, $b_4 = 1969.8$.

CONCLUSIONS

This study presents the modeling and implementation of four-bar mechanism for realizing humanoid neck. The dynamics of head mechanism were studied by deriving the equations from the basic laws for rotary actuators in order to correlate all the variables that play important role towards the time response of neck mechanism. Low cost RC servo motors have been previously deployed for mimicking human motion; however, the performance of such motors along with a kinematic chain has not been analyzed. Thus, a thorough review of neck designs was conducted to arrive at robust neck design and mathematical relationships were derived to predict its performance. Results indicate that the neck mechanism presented here attains the performance similar to that of human neck when RC servo motor uses an external PD controller to reduce the inherent overshoot found in dynamical systems. The specific contributions of this study are: (i) a method to set parameters of neck with a four-bar mechanism to meet specific desired characteristics; (ii) modeling of the combinatory system consisting of servomotor, four-bar mechanism, irregular-shaped robotic head to realize neck mechanism, and a simplification thereof, (iii) the modeling and experimental investigation of the performance of RC servo motor in humanoid neck design, and (iv) a procedure for building the humanoid neck mechanism. The primary objective has been to keep the 'costs' low both in terms of material as well as design complexity.

ACKNOWLEDGMENT

This research was fully supported by Automation and Robotics Research Institute, Fort Worth, TX and NSF phase I SBIR grant. The authors at Virginia Tech would also like to acknowledge the support from Office of Naval Research (ONR) and ICTAS.

REFERENCES

Albers, A., Brudniok, S. and Burger, W. 2003. "The Mechanics of a Humanoid," In: *Proceedings of IEEE Humanoids(Humanoid 2003)*, Karlsruhe, Germany.

Albers, A., Brudniok, S. and Burger, W. 2004. "Design and Development Process of a Humanoid Robot Upper Body through Experimentation," In: *4th IEEE/RAS International Conference on Humanoid Robots*, 10–12 November, Los Angeles, CA, Vol. 1, pp. 77–92.

Ambrose, R.O., Aldridge, H., Askew, R.S., Burridge, R.R., Bluethmann, W., Diffler, M., Lovchik, C., Magruder, D. and Rehnmark, F. 2000. "Robonaut: NASA's Space Humanoid," *IEEE Intelligent Systems and their Applications*, 15:57–63.

Analog Devices. 2010. Available at: http://www.analog.com (accessed date February 15, 2010).

An, J. and Kwon, D.S. 2009. "Five-bar Linkage Haptic Device with DC Motors and MR Brakes," *Journal of Intelligent Material Systems and Structures*, 20:97–107.

Ashrafiuon, H., Eshraghi, M. and Elahinia, M.H. 2006. "Position Control of a Three-link Shape Memory Alloy Actuated Robot," *Journal of Intelligent Material Systems and Structures*, 17:381–392.

Backaitis, S.H. 1993. *Biomechanics of Impact Injury and Injury Tolerances of the Head-Neck Complex*, Society of Automotive Engineers, Inc., Warrendale, PA.

Bedogni, G., Malavolti, M., Severi1, S., Poli1, M., Mussi, C., Fantuzzi, A.L. and Battistini, N. 2002. "Accuracy of an Eight-point Tactile-electrode Impedance Method in the Assessment of Total Body Water," *European Journal of Clinical Nutrition*, 56:1143–1148.

Berns, K. and Braum, T. 2005. "Design Concept of a Human-like Robot Head," In: *Proceedings of 5th IEEE-RAS International Conference on Humanoid Robots*, 5 December, USA, pp. 32–37.

Berns, K., Hillenbrand, C. and Mianowski, K. 2006. *The Mechatronic Design of a Human-like Robot Head*, Courses and Lectures–International Center for Mechanical Sciences, pp. 263–270, Springer-Verlag, New York.

Berns, K. and Hirth, J. 2006. "Control of Facial Expressions of the Humanoid Robot Head ROMAN," In: *Proceeding of IEEE/RSJ International Conference on Intelligent Robots and Systems*, 9–15 October, Beijing, China, pp. 3119–3124.

Breazeal, C. 2004. "Function Meets Style: Insights from Emotion Theory Applied to HRI," *IEEE Transactions on Systems, Man, and Cybernetics, Part C: Applications and Reviews*, 34:187–194.

Brooks, R.A., Breazeal, C., Marjanovic, M., Scassellati, B. and Illiamson, M. 1998. "The Cog Project: Building a Humanoid Robot," In: Nehaniv, C. (ed.), The Cog Project: Building a Humanoid Robot," *Computation for Metaphors, Analogy, and Agents* Lecture Notes in Artificial Intelligence, Vol. 1562, 52–87.

DC Micromotors. 2010. Available at: http://www.directindustry.com/industrial-manufacturer/dc-micro-motor-72490.html (accessed date February 15, 2010).

Goyal, S.C. and Bakshi, U.A. 2007. *Control Systems Engineering*, Technical Publications Pune, Pune, India.

Guenter, F., Roos, L., Guignard, A. and Billard, A.G. 2005. "Design of a Biomimetic Upper Body for the Humanoid Robot Robota," In: *Proceedings of 5th IEEE/RAS International Conference on Humanoid Robots*, 05 December, USA, pp. 56–61.

Han, J.D., Zeng, S.Q., Tham, K.Y., Badgero, M. and Weng, J.Y. 2002. "Dav: A Humanoid Robot Platform for Autonomous Mental Development," In: *Proceeding of IEEE 2nd International Conference on Development and Learning (ICDL 2002)*, 12–15 June, MIT, Cambridge, MA, pp. 73–81.

Hanson Robotics Inc. 2009. Available at: www.hansonrobotics.com (accessed date June 22, 2009).

Hanson, D., Bergs, R., Tadesse, Y., White, V. and Priya, S. 2006. "Enhancement of EAP Actuated Facial Expressions by Designed Chamber Geometry in Elastomers," In: *Proceedings of SPIE Smart Structures and Materials*, 27 February, San Deigo, CA, Vol. 6168, pp. 1–9.

Hashimoto, T., Hitramatsu, S., Tsuji, T. and Kobayashi, H. 2006. "Development of the Face Robot SAYA for Rich Facial Expressions," In: *SICE-ICASE, International Joint Conference*, 18–21 October, Bexco, Busan, Korea, pp. 5423–5428.

Heymsfield, S.B., Arteaga, C., McManus, C., Smith, J. and Moffitt, S. 1983. "Measurement of Muscle Mass in Humans: Validity of the 24-hour Urinary Creatinine Method," *American Journal of Clinical Nutrition*, 37:478–494.

Huang, Y. 2000. "3D Motion Estimation of Head and Shoulders in Videophone Sequences," In: *Proceedings of IEEE International Conference on Communication Technology, WCC – ICCT 2000*, 21–25 August, Beijing, China, Vol. 2, pp.1180–1183.

Huelke, D.F. 1979. "Anatomy of the Human Cervical Spine and Associated Structures," In: *The Human Neck-Anatomy, Injury Mechanisms and Biomechanics*, pp. 1–7, Society of Automotive Engineers Inc., Warrendale, PA.

Jamone, L., Metta, G., Nori, F. and Sandini, G. 2006. "James: A Humanoid Robot Acting over an Unstructured World," In: *Proceedings* of *6th IEEE/RAS International. Conference on Humanoid Robots*, 4–6 December, Genoa, pp. 143–150.

Kawano, H., Ando, H., Hirahara, T., Yun, C. and Ueha, S. 2005. "Application of a Multi-DOF Ultrasonic Servomotor in an Auditory Tele-existence Robot," *IEEE Transactions on Robotics and Automation*, 21:790–800.

Kulakowski, B.T., Gardner, J.F. and Shearer, J.L. 2007. *Dynamic Modeling and Control of Engineering Systems*, 3rd edn, Cambridge University Press, New York.

Lanteigne, E. and Jnifene, A. 2008. "An Experimental Study on a SMA Driven Pressurized Hyper-Redundant Manipulator," *Journal of Intelligent Material Systems and Structures*, 19:1067–1076.

Lee, S.H. and Terzopoulos, D. 2006. "Heads Up! Biomechanical Modeling and Neuromuscular Control of the Neck," *ACM Transactions on Graphics* 25: 1188–1198.

Mai, J., Cheng-Tao, C., Qi-Dan, Z. and Zhen, S. 2009. "Helicopter Rotors Pyramid Angle Measurement Based on CMOS Technology," In: *IEEE Chinese Control and Decision Conference, CCDC'09*, 17–19 June, Guilin, China, pp. 4369–4374.

Mertz, H.J. and Patrick, L.M. 1993. "Investigation of the Kinematics and Kinetics of Whiplash during Vehicle Rear-end Collisions," In: Backaitis, H.S. (ed.), *Biomechanics of Impact Injury and Injury and Injury Tolerances of the Head-Neck Complex*, pp. 43–71, Society of Automotive Engineers Inc., Warrendale, PA, USA.

Milecki, A. and Sedziak, D. 2005. "The Use of Magnetorheological Fluid Dampers to Reduce Servo Drive Velocity Jumps due to Load Changes," *Journal of Intelligent Material Systems and Structures*, 16:501–510.

Miwa, H., Okuchi, T., Itoh, K., Takanobu, H. and Takanishi, A. 2003. "A New Mental Model for Humanoid Robots for Human Friendly Communication, Introduction of Learning System, Mood Vector and Second Order Equations of Emotion," In: *Proceedings of ICRA '03. IEEE International Conference on Robotics and Automation*, 14–19 September, Taipei, Taiwan, Vol. 3, pp. 3588–3593.

Oh, J.H., Hanson, D., Kim, W.S., Han, Y., Kim, J.Y. and Park, I.W. 2006. "Design of Android Type Humanoid Robot Albert HUBO," In: *Proceedings of IEEE/RSJ International Conference on Intelligent Robots and Systems*, 09–15 October, Beijing, China, pp. 1428–1433.

Ouerfelli, M., Kumar, V. and Harwin, W.S. 1999. "Kinematic Modeling of Head-Neck Movements," *IEEE Transactions on Systems, Man and Cybernetics*, 29:604–615.

Ouezdou, F.B., Alfayad, S., Pirim, P. and Barthelemy, S. 2006. "Humanoid Head Prototype with Uncoupled Eyes and Vestibular Sensors," In: *Proceedings* of *IEEE/RSJ International Conference on Intelligent Robots and Systems*, 09–15 October, Beijing, China, pp. 2980–2985.

Patane, F., Laschi, C., Miwa, H., Guglielmelli, E., Dario, P. and Takanishi, A. 2004. "Design and Development of a Biologically-inspired Artificial Vestibular System for Robot Heads," In: *Proceedings of IEEE/RSJ International Conference on Intelligent Robots and Systems(IROS 2004)*, 28 September–2 October, Sendal, Japan, Vol. 2, pp. 1317–1322.

Pedrocchi, A. and Ferrigno, G. 2004. "Model of Head-Neck Joint Fast Movements in the Frontal Plane," *Biological Cybernetics*, 90:377–389.

Rose, M., Keimer, R., Breitbach, E.J. and Campanile, L.F. 2004. "Parallel Robots with Adaptronic Components," *Journal of Intelligent Material Systems and Structures*, 15:763–769.

Rudenko, O.V. and Sarvazyan, A.P. 2006. "Wave Biomechanics of the Skeletal Muscle," *Acoustical Physics*, 52:720–732.

Sabater, J.M., Garcia, N., Perez, C., Azorin, J.M., Saltaren, R.J. and Yime, E. 2006. "Design and Analysis of a Spherical Humanoid Neck using Screw Theory," In: *Proceedings of 1st IEEE/RAS-EMBS International Conference on Biomedical Robotics and Biomechatronics*, 20–22 February, Pisa, Italy, pp. 1166–1171.

Saga, N. 2007. "Development of a Tendon Driven System using a Pneumatic Balloon," *Journal of Intelligent Material Systems and Structures*, 18:171–174.

Saito, T. and Ikeda, H. 2007. "Development of Normally Closed Type of Magnetorheological Clutch and its Application to Safe Torque Control System of Human-Collaborative Robot," *Journal of Intelligent Material Systems and Structures*, 18:1181–1185.

Sakagami, Y., Watanabe R., Aoyama, C., Matsunaga, S., Higaki, N. and Fujimura, K. 2002. "The Intelligent ASIMO: System Overview and Integration," In: *Proceedings of IEEE/RSJ International Conference on Intelligent Robots and Systems,* 30 September–5 October, Lausanne, Switzerland, Vol.3, pp. 2478–2483.

Sharkey, P.M., Murray, D.W. and Heuring, J.J. 1997. "On the Kinematics of Robot Heads," *IEEE Transactions on Robotics and Automation*, 13:437–442.

Shimada, M., Minato, T., Itakura, S. and Ishiguro, H. 2006. "Evaluation of Android using Unconscious Recognition," In: *Proceedings of 6th IEEE-RAS International Conference on Humanoid Robots*, 04–06 December, Genoa, Italy, pp. 157–162.

Spexard, T.P., Hanheide, M. and Sagerer, G. 2007. "Human-oriented Interaction with an Anthropomorphic Robot," *IEEE Transactions on Robotics and Automation*, 23:852–862.

Spiess, S. and Vincze, M. 1998. "Comments on "On the Kinematics of Robot Heads," *IEEE Transactions on Robotics and Automation*, 14:509–510.

Tadesse, Y., Bergs, R., Priya, S., Stephanou, H., Popa, D. and Hanson, D. 2006. "Piezoelectric Actuation and Sensing for Facial Expression Robotics," *Ferroelectrics*, 345:13–25.

Tadesse, Y. and Priya, S. 2008. "Humanoid Face Utilizing Rotary Actuators and Piezoelectric Sensors," In: *Proceedings of IMECE2008, Mechanics of Solids, Structures and Fluids/Recent Advances in Engineering Applications,* 31 October–6 November, Boston, Massachusetts, USA, Vol. 12, pp. 573–581.

Tiejun, Z., Dalong, T. and Mingyang, Z. 2005. "The Development of a Mobile Humanoid Robot with Varying Joint Stiffness Waist," In: *Proceedings* of *IEEE International Conference on Mechatronics and Automation*, 29 July to 01 August, Niagara Falls, Ontario, Canada, Vol. 3, pp. 1402–1407.

Toshima, I., Uematsu, H. and Hirahara, T. 2003. "A Steerable Dummy Head that Tracks Three-Dimensional Head Movement: TeleHead," *Acoustical Science and Technology*, 24:327–329.

Wang, Z., Deurenberg, P., Wang, W., Pietrobelli, A., Baumgartner, R. and Heymsfield, S. 1999. "Hydration of Fat-free Body Mass: Review and

Critique of a Classic Body-Composition Constant," *American Journal of Clinical Nutrition*, 69:833–841.

Wiguna, T., Heo, S., Park, H.C. and Goo, N.S. 2009. "Design and Experimental Parameteric Study of a Fish Robot Actuated by Piezoelectric Actuators," *Journal of Intelligent Material Systems and Structures*, 20:751–758.

Yan, S., Liu, X., Xu, F. and Wang, J. 2007. "A Gripper Actuated by a Pair of Differential SMA Springs," *Journal of Intelligent Material Systems and Structures*, 18:459–466.

Yao, J. and Taylor, R. 2003. "Assessing Accuracy Factors in Deformable 2D/3D Medical Image Registration using a Statistical Pelvis Model," In: *Proceedings of 9th IEEE International Conference on Computer Vision*, 13–16 October, Nice, France, Vol. 2, pp. 1329–1334.

Yuan, J. and Long, X. 2003. "CCD-Area-based Autocollimator for Precision Small-Angle Measurement," *Review of Scientific Instruments*, 74:1362–1365.

Zafar, H., Nordh, E. and Eriksson, P.O. 2002. "Spatiotemporal Consistency of Human Mandibular and Head-Neck Movement Trajectories during Jaw Opening-Closing Task," *Experimental Brain Research*, 146:70–76.